1 **10–year satellite–constrained fluxes of ammonia improve**

2 **performance of chemistry transport models**

4 **Nikolaos Evangeliou[1,*], Yves Balkanski[2], Sabine Eckhardt[1], Anne Cozic[2], Martin**

5 **Van Damme[3], Pierre-François Coheur[3], Lieven Clarisse[3], Mark W. Shephard[4],**

6 **Karen E. Cady-Pereira[5], Didier Hauglustaine[2]**

8 [1]Norwegian Institute for Air Research (NILU), Department of Atmospheric and Climate

9 Research (ATMOS), Kjeller, Norway.

10 [2]Laboratoire des Sciences du Climat et de l'Environnement (LSCE), CEA-CNRS-UVSQ,

11 91191, Gif-sur-Yvette, France.

12 [3]Université libre de Bruxelles (ULB), Spectroscopy, Quantum Chemistry and Atmospheric

13 Remote Sensing (SQUARES), Brussels, Belgium.

14 [4]Environment and Climate Change Canada, Toronto, Ontario M3H 5T4, Canada.

15 [5]Atmospheric and Environmental Research, Inc., Lexington, MA, USA.

17 ***** Corresponding author: N. Evangeliou (Nikolaos.Evangeliou@nilu.no)

Abstract

In recent years, ammonia emissions have been continuously increasing being almost four times higher than in the 20th century. Although an important species as its use as a fertilized sustains human living, ammonia has major consequences both for humans and the environment, because of its reactive gas phase chemistry that makes it easily convertible to particles. Despite its pronounced importance, yet, ammonia emissions are highly uncertain in most emission inventories. However, the great development of satellite remote sensing nowadays provides the opportunity for more targeting research in constraining ammonia emissions. Here, we used satellite measurements to calculate global ammonia emissions over the period 2008–2017. Then, the calculated ammonia emissions were fed to a chemistry transport model and ammonia concentrations were simulated for the period 2008–2017.

The simulated concentrations of ammonia were compared with ground measurements from Europe, North America and Southeastern Asia, as well as with satellite measurements. The satellite-constrained ammonia emissions represent global concentrations more accurately than state-of-the-art emissions. Calculated fluxes in the North China Plain were seen more increased after 2015, not due to emission changes, but due to changes in sulfate emissions that resulted in less ammonia neutralization and hence in larger atmospheric loads. Emissions over Europe were also twice as much as those in traditional datasets with dominant sources to be industrial and agricultural applications. Four hot-spot regions of high ammonia emissions were seen in North America characterized by large agricultural activity, animal breeding, animal farms and animal breeding and agricultural practices. South America is dominated by ammonia emissions from biomass burning, which cause a strong seasonality. In Southeastern Asia, ammonia emissions from fertilizer plants in China, Pakistan, India and Indonesia are the most important, while a strong seasonality was observed with a spring and late summer peak due to rice and wheat cultivation. Measurements of ammonia surface concentrations were better reproduced with satellite-constrained emissions, so as measurements from CrIS (Cross-track Infrared Sounder).

1 Introduction

Ammonia (NH_3) has received a lot of attention nowadays due to its major implications for the population and the environment (Erisman, 2004; Erisman et al., 2007). These include eutrophication of semi-natural ecosystems and acidification of soils (Stevens et al., 2010), secondary formation of particulate matter in the atmosphere (Anderson et al., 2003), and alteration of the global greenhouse balance (De Vries et al., 2011). More specifically in the troposphere, ammonia reacts with the abundant sulfuric and nitric acids (Malm, 2004) contributing 30 % to 50 % of the total aerosol mass of PM2.5 and PM10 (Anderson et al., 2003). Ammonium aerosols are therefore a very important component in regional and global aerosols processes (Xu and Penner, 2012) also having significant implications for human health (Aneja et al., 2009). Ammonia alters human health indirectly mainly through formation of PM2.5 (Gu et al., 2014) that penetrate the human respiratory systems and deposit in the lungs and alveolar regions (Pope III et al., 2002) causing premature mortality (Lelieveld et al., 2015). As regards to the climate impact, the same ammonium aerosol particles affect Earth's radiative balance, both directly by scattering incoming radiation (Henze et al., 2012) and indirectly as cloud condensation nuclei (Abbatt et al., 2006). They may also cause visibility problems and contribute to haze effect due to secondary PM formation.

Sources of ammonia include wild animals (Sutton et al., 2000), ammonia-containing watersheds (Sørensen et al., 2003), traffic (Kean et al., 2009), sewage systems (Reche et al., 2012), humans (Sutton et al., 2000), biomass burning (Sutton et al., 2008) and domestic coal combustion (Fowler et al., 2004), volcanic eruptions (Sutton et al., 2008) and agriculture (Erisman et al., 2007). The latter is responsible for the majority of ammonia global atmospheric emissions. Specifically, in the United States and Europe about 80% of all emissions is related to agriculture (Leip et al., 2015). Emissions have increased considerably since pre-industrial times and are unlikely to decrease due to the growing demand for food and feed (Aneja et al., 2008).

The growing attention in ammonia levels has enabled many monitoring actions in Europe (European Monitoring and Evaluation Programme, EMEP), in Southeastern Asia (East Asia acid deposition NETwork) and in the North America (Ammonia Monitoring Network in the US, AMoN-US; National Air Pollution Surveillance Program (NAPS) sites in Canada) to record surface concentrations of ammonia continuously. Recently, several satellite products have been also developed in an effort to identify global levels of ammonia considering that the

79   relatively sparse existing monitoring network has an insufficient coverage for this purpose.
80   These are derived from satellite sounders as the Infrared Atmospheric Sounding Interferometer
81   (IASI) (Van Damme et al., 2017), the Atmospheric Infrared Sounder (AIRS) (Warner et al.,
82   2017), the Cross-track Infrared Sounder (CrIS) (Shephard and Cady-Pereira, 2015), the
83   Tropospheric Emission Spectrometer (TES) (Shephard et al., 2015), and Greenhouse Gases
84   Observing Satellite (Someya et al., 2020). Both IASI and CrIS ammonia products are being
85   continuously compared and evaluated against other observations and products. Relevant
86   analyses include comparison against column-integrated levels measured by Fourier transform
87   infrared spectroscopy (FTIR) (Dammers et al., 2016, 2017), ground-based measurements (Van
88   Damme et al., 2015; Kharol et al., 2018), bottom-up emissions (Van Damme et al., 2018;
89   Dammers et al., 2019) and atmospheric chemistry transport models (CTMs) (Shephard et al.,
90   2020; Whitburn et al., 2016a).

91   Despite its importance, ammonia is a poorly quantified trace gas, with uncertainties over
92   50% on the global emission budget and even higher on temporal and local scales (Dentener and
93   Crutzen, 1994; Faulkner and Shaw, 2008; Reis et al., 2009) and up to 300% for the agricultural
94   sector in Europe (European Environment Agency, 2019). In the present paper, we grid 10 years
95   (2008–2017) of satellite measurements of ammonia retrieved from IASI to calculate monthly
96   surface emissions (hereafter named NE) (see section 2). The same is done using the gridded
97   IASI ammonia column concentrations from Van Damme et al. (2018) (named as VD0.5 and
98   VDgrlf) (see section 2). The three different emission inventories together with a state–of–the–
99   art one, which is more often used by models (named as EGG), are then imported in a CTM to
100   simulate ammonia for the same 10–year period. More details of the different emissions used
101   here are shown in sections 2.4 and 2.1. Finally, an evaluation of simulated surface
102   concentrations against ground–based measurements from different monitoring stations and
103   satellite products allow to quantify the improvements in ammonia emissions.

2   Methods

2.1   LMDz-OR-INCA chemistry transport model

106   The Eulerian global CTM LMDz-OR-INCA was used to calculate ammonia lifetime, as
107   well as to simulate ammonia concentrations from the emission fluxes calculated from IASI
108   satellite products. The model couples the LMDz (Laboratoire de Météorologie Dynamique)
109   General Circulation Model (GCM) (Hourdin et al., 2006) with the INCA (INteraction with
110   Chemistry and Aerosols) model (Folberth et al., 2006; Hauglustaine et al., 2004) and with the

land surface dynamical vegetation model ORCHIDEE (ORganizing Carbon and Hydrology In Dynamic Ecosystems) (Krinner et al., 2005). In the present configuration, the model has a horizontal resolution of $2.5° \times 1.3°$, the vertical dimension is divided into 39 hybrid vertical levels extending to the stratosphere. Large-scale advection of tracers is calculated from a monotonic finite-volume second-order scheme (Hourdin and Armengaud, 1999), deep convection is parameterized according to the scheme of Emanuel, (1991), while turbulent mixing in the planetary boundary layer (PBL) is based on a local second-order closure formalism. More information and a detailed evaluation of the GCM can be found in Hourdin et al. (2006).

The model simulates atmospheric transport of natural and anthropogenic aerosols recording both the number and the mass of aerosols. The aerosol size distribution is represented using a modal approach that consists of the superposition of 5 log-normal modes that represent both the size spectrum and whether the aerosol is soluble or insoluble (Schulz, 2007). The aerosols are treated in three particle modes, sub-micronic (diameter < 1 μm) corresponding to the accumulation mode, micronic (diameter 1–10 μm) corresponding to coarse particles, and super-micronic or super coarse particles (diameter > 10 μm). LMDz-OR-INCA accounts for emissions, transport (resolved and sub-grid scale), and dry and wet (in-cloud/below-cloud scavenging) deposition of chemical species and aerosols interactively. LMDz-OR-INCA includes a full chemical scheme for the ammonia cycle and nitrate particle formation, as well as a state-of-the-art $CH_4/NO_x/CO/NMHC/O_3$ tropospheric photochemistry. Further details about specific reactions, reaction rates and other information entering into the description of the ammonia cycle can be found in Hauglustaine et al. (2014).

The global transport of ammonia was simulated from 2007 to 2017 (2007 was the spin-up period) by nudging the winds of the 6-hourly ERA Interim Reanalysis data (Dee et al., 2011) with a relaxation time of 10 days (Hourdin et al., 2006). For the calculation of ammonia's lifetime, the model ran with traditional emissions for anthropogenic, biomass burning and oceanic emission sources using emissions from ECLIPSEv5 (Evaluating the CLimate and Air Quality ImPacts of Short-livEd Pollutants), GFED4 (Global Fire Emission Dataset) and GEIA (Global Emissions InitiAtive) (hereafter called EGG) (Bouwman et al., 1997; Giglio et al., 2013; Klimont et al., 2017).

2.2 Satellite ammonia

2.2.1 IASI ammonia

The Infrared Atmospheric Sounding Interferometer (IASI) onboard the MetOp-A satellite measures Earth's infrared radiation twice a day in a spectral range of 645–2,760 cm^{-1} with an elliptical footprint with a diameter of 12 km at nadir (Clerbaux et al., 2009). Due to the larger thermal conditions that lead to smaller uncertainties, only morning data were used in the present assessment (Clarisse et al., 2010). Van Damme et al. (2018) reported limited impact of the IASI overpasses of 4%±8% on ammonia. The 10–year dataset used here is ANNI-NH3-v2.1R-I product (Van Damme et al., 2017) and relies on ERA-Interim ECMWF meteorological input data (Dee et al., 2011). The Artificial Neural Network for IASI (ANNI) algorithm converts the hyperspectral range index to an column–integrated NH$_3$ value (Whitburn et al., 2016a). The latter relies on the fact that the indices can be converted to a column by taking into account the spectral sensitivity to the ammonia abundance in the observed scene. The hyperspectral range indexes are derived from linear retrievals using a constant gain matrix which includes a generalized error covariance matrix (Van Damme et al., 2014b; Whitburn et al., 2016a). The dataset also provides cloud coverage for each measurement (August et al., 2012). Only measurements with a cloud fraction below 10% were processed in consistency with Van Damme et al. (2018). Cloud coverage was not provided for all measurements until March 2010 resulting in smaller data availability before that date. Van Damme et al. (2014a) reported that IASI better measures ammonia in spring and summer months, due to the strong dependence on thermal contrast (error below 50%). For an individual observation, an IASI-retrieved column is considered detectable when the vertical column density exceeds 9.68×10^{15} molecules cm^{-2} (surface concentration > 1.74 μg m^{-3}) at a thermal contrast of 20 K, while the vertical column density should be larger than 1.69×10^{16} molecules cm^{-2} (3.05 μg m^{-3}) at 10 K (Van Damme et al., 2014a). Although the retrieval algorithm uses a fixed vertical profile, extended validation of the resulting dataset has verified small uncertainties (Van Damme et al., 2015, 2018; Dammers et al., 2016; Whitburn et al., 2016b). For instance, Van Damme et al. (2018) reported a difference of 2%±24% (global average) in column–integrated ammonia using different vertical profiles in the retrieval algorithm.

2.2.2 CrIS ammonia

The Cross-Track Infrared Sounder (CrIS) was first launched on the NASA Suomi National Polar-orbiting Partnership (S-NPP) satellite on 28 October 2011 in a sun-synchronous low Earth orbit. The CrIS sensor provides soundings of the atmosphere with a spectral

resolution of 0.625 cm^{-1} (Shephard et al., 2015). One of the main advantages of CrIS is its improved vertical sensitivity of ammonia closer to the surface due to the low spectral noise of ~0.04K at 280K in the NH$_3$ spectral region (Zavyalov et al., 2013) and the early afternoon overpass that typically coincides with high thermal contrast, which is optimal for thermal infrared sensitivity. The CrIS Fast Physical Retrieval (CFPR) (Shephard and Cady-Pereira, 2015) retrieves an ammonia profile (14 levels) using a physics-based optimal estimation retrieval, which also provides the vertical sensitivity (averaging kernels) and an estimate of the retrieval errors (error covariance matrices) for each measurement. As peak sensitivity is typically in the boundary layer between 900 and 700 hPa (~ 1 to 3 km) (Shephard et al., 2020), the surface and total column concentrations are both highly correlated with the retrieved levels in the boundary layer. Shephard et al. (2020) reports estimated total column random measurement errors of 10–15%, with estimated total random errors of ~30%. The individual profile retrieval levels have estimated random measurement errors of ~10 to 30 %, with estimated total random errors increasing to 60 to 100% due to the limited vertical resolution. These vertical sensitivity and error output parameters are also useful for using CrIS observations in applications (e.g. data fusion, data assimilation; model-based emission inversions (e.g., Cao et al., 2020; Li et al., 2019) as a satellite observational operator can be generated in a robust manner. The detection limit of CrIS measurements has been calculated down to 0.3–0.5 ppbv (Shephard et al., 2020). CrIS ammonia has been evaluated against other observations over North America with the Ammonia Monitoring Network (AMoN) (Kharol et al., 2018) and against ground-based Fourier transform infrared (FTIR) spectroscopy observations (Dammers et al., 2017) showing small differences and high correlations.

2.3 Inverse Distance Weighting (IDW) interpolation

To process large amounts of measurements in a 2-dimensional grid of high resolution, oversampling methods (Streets et al., 2013) can be used (Van Damme et al., 2018). However, considering that the resolution of the CTM is 2.5°×1.3° (see section 2.4), there is no need to process the measurements on such a high-resolution grid and therefore an interpolation method was used. The method has been extensively used after the Chernobyl accident in 1986 to process more than 500 thousand deposition measurements over Europe (De Cort et al., 1998; Evangeliou et al., 2016).

IASI total column ammonia measurements were interpolated onto a grid of 0.5°×0.5° using a modified Inverse Distance Weighting (IDW) algorithm described by (Renka, 1988).

206 This method is preferred due to its ease of use and to its high quality of interpolation. The IDW
207 interpolation is defined by:

208 $$\hat{v}(x,y) = \frac{\sum_{i=1}^{n} w_i v_i}{\sum_{i=1}^{n} w_i} \qquad \textbf{Eq. 1}$$

209 where $\hat{v}(x,y)$ is the interpolated value at point (x,y), $w_1, ..., w_i$ are the relative weights and
210 $v_1, ..., v_n$ are the observation values. The weights are defined by the inverse distance functions:

211 $$w_i = \left(\frac{(r_w - d_i)}{r_w d_i}\right)^2 \qquad \textbf{Eq. 2}$$

212 $$\text{for } (r_w - d_i) = \begin{cases} r_w - d_i \, if \, d_k < r_w, \\ 0 \, if \, d_k \geq r_w. \end{cases}$$

213 where r_w denotes the radius of influence of the point (x_i, y_i), d_i the Euclidean distance
214 between point (x,y) and (x_i, y_i), and d_k is the threshold distance. We used a threshold
215 distance (d_k) of 50 km, which is similar to the size of each grid cell; different d_k values were
216 included in a sensitivity study (see section 4.2). The Euclidean distance is calculated using
217 Vincenty's formulae (Vincenty, 1975). Finally, the gridded IASI total column ammonia was re-
218 gridding to the model resolution (2.5°×1.3°) using bilinear interpolation.

219 ## 2.4 Emission flux calculation of ammonia

220 The emission fluxes of ammonia were calculated using a 1–dimensional box model that
221 assumes first-order loss terms for ammonia and has been already used previously (Van Damme
222 et al., 2018; Whitburn et al., 2016b). It takes into account the gridded column concentrations of
223 ammonia that were calculated with the IDW interpolation method and all the potential removal
224 processes of ammonia occurring in a hypothetical atmospheric box according to the following
225 equation:

226 $$E_{NH3} = M_{NH3} / \tau \qquad \textbf{Eq. 3}$$

227 where M_{NH3} is the mass of ammonia in each atmospheric box (grid-cell) in molecules cm^{-2} and
228 τ is the lifetime of ammonia in the box (given in seconds).

229 Van Damme et al. (2018) assumed a constant lifetime for ammonia, admitting that this is
230 a limiting factor of their study on the basis that chemical loss and deposition are highly variable
231 processes that can change the lifetime drastically. To tackle the large variability of the lifetime
232 of ammonia, we used monthly gridded lifetime calculated from a CTM. This gives robustness
233 in the calculated emissions fluxes considering that at regions where sulfuric and nitric acids are
234 abundant, the chemical loss will be more intensive and, thus, lifetime will be much shorter
235 affecting emissions dramatically.

The lifetime (τ) of ammonia in each grid-box results from the three processes affecting ammonia concentrations: transport (t_{trans}) in and out of the grid-cell, chemical loss (t_{chem}) and deposition (t_{depo}):

$$\frac{1}{\tau} = \frac{1}{t_{trans}} + \frac{1}{t_{chem}} + \frac{1}{t_{depo}} \qquad \textbf{Eq. 4}$$

In a CTM, the lifetime can be easily calculated from the species mass balance equation (Croft et al., 2014):

$$\frac{dC(t)}{dt} = S(t) - \frac{C(t)}{\tau(t)} \qquad \textbf{Eq. 5}$$

where $C(t)$ is the atmospheric burden of ammonia at time t, $S(t)$ is the time-dependent source emission fluxes and $\tau(t)$ is the removal timescale. Assuming steady-state conditions and considering that emission fluxes of ammonia are continuous, there is a quasi-equilibrium between sources and removals of ammonia (Dentener and Crutzen, 1994), and the modeled lifetime of ammonia τ_{mod} can be defined as:

$$\tau_{mod} = {C_{NH3}} \Big/ {L_{NH3}^{trans,chem,depo}} \qquad \textbf{Eq. 6}$$

where C_{NH3} is the atmospheric burden of ammonia and $L_{NH3}^{trans,chem,depo}$ is the total loss due to any process affecting ammonia in the model (transport, chemical reactions, deposition).

We calculate ammonia emission fluxes using IASI satellite measurements that we interpolated (see section 2.3) to the model resolution (2.5°×1.3°) and applying a variable lifetime taken from a CTM (hereafter NE emissions). We also calculate ammonia emissions from the oversampled IASI data of Van Damme et al. (2018), after bilinear re-gridding to the model resolution (2.5°×1.3°), applying a constant lifetime for ammonia of 12 hours (hereafter VD0.5 emissions) and the same variable lifetime from a CTM as in the NE emissions (hereafter VDgrlf emissions).

3 Results

In this section, the main results of the monthly emissions (NE) are presented for the 10-year period (2008–2017) of IASI observations. We first describe the monthly modelled ammonia lifetimes (section 3.1). Then, we explain the main characteristics of the obtained emissions (section 3.2) and compare them with those calculated using the IASI gridded products from Van Damme et al. (2018) (VD0.5 and VDgrlf), as well as the ones from the state-of-the-art inventories of EGG and EDGARv4.3.1-GFED4 (Crippa et al., 2016; Giglio et al.,

265 2013) that are often used in CTMs (section 3.3). We finally turn our focus to emissions at
266 continental regions and document their seasonal variation in emissions (section 3.4).

3.1 Modelled lifetime of ammonia

268   The lifetime of ammonia has been reported to range from a few hours to a few days
269 (Behera et al., 2013; Pinder et al., 2008) so ammonia can only be transported over relatively
270 short distances. This short spread of ammonia is also due to the fact that (a) the majority of its
271 emissions are surface ones (major source is agricultural activity), and (b) its surface deposition
272 velocities are high for most surfaces (Hov et al., 1994). The atmospheric lifetimes of ammonia
273 were summarized in Van Damme et al. (2018). Specifically, Quinn et al. (1990) and more
274 recently Norman and Leck (2005) reported lifetimes of a few hours in the West Pacific, South
275 Atlantic and Indian Oceans, which is in agreement with Flechard and Fowler (1998), who
276 reported a 2-hour lifetime in an area of Scotland where most sources are of agricultural origin.
277 Similar to them, Dammers et al. (2019) recently reported a lifetime estimated from satellite
278 measurements of 2.35±1.16 hours for large point sources based on satellite measurements. The
279 majority of ammonia lifetimes reported regionally or globally fall within 10 and 24 hours
280 independently of the different approaches (Hauglustaine et al., 2014; Hertel et al., 2012; Möller
281 and Schieferdecker, 1985; Sutton et al., 1993; Whitburn et al., 2016b), while Dentener and
282 Crutzen (1994) reported slightly higher lifetimes within a range between 0.9 and 2.1 days
283 depending on ammonia emission fraction of natural origin. Monthly averaged atmospheric
284 ammonia lifetimes in the present study were derived using the version of the LMDz-OR-INCA
285 that includes non-methane hydrocarbons (Hauglustaine et al., 2004).

286   Ammonia lifetime depends on numerous factors such as the presence of ammonia's
287 reactants (sulfuric and nitric acids, through SO_2 and NO_x emissions), meteorological parameters
288 (atmospheric water vapour, and temperature, atmospheric mixing and advection) and ammonia
289 emissions. In ammonia–poor conditions, all ammonia is rapidly removed by neutralising
290 sulfuric acid with an intermediate production of bisulfate. If ammonia increases further
291 (ammonia–rich conditions), then reaction with nitric acid occurs forming nitric ammonium. At
292 this point, the ammonia/sulfuric acid/nitric acid equilibrium becomes very fragile. If sulfate
293 concentrations decrease, then free ammonia is produced, which gradually reacts with nitric acid
294 resulting in production of aerosol phase nitric ammonium. But if particles are aqueous, then
295 sulfate ions in solution increase the equilibrium vapour pressure of ammonia with nitric acid
296 reversing the reaction towards gaseous phase reactants. So, sulfate reductions are linked with

297 non-linear increases of aerosol nitrates and decreases of aerosol ammonium and water (Seinfeld

298 and Pandis, 2000).

299 The calculated ammonia lifetime is shown in **Figure 1**a averaged for the whole study

300 period. The average lifetime was calculated to be 11.6±0.6 hours, which is in the range of the

301 previously reported values. Lower values (~10 hours) were observed in clean remote areas

302 characterized by low ammonia emissions (e.g., Amazon forest, Sahara and Australia), while in

303 the rest of the globe the lifetime was closer to the average value. The highest lifetimes (~16

304 hours) occur over Southern Brazil and Venezuela, which are both areas with relatively high

305 ammonia emissions and low sulfuric and nitric acid concentrations (**Figure 1**c). These

306 conditions are characterized by a low atmospheric sulfuric and nitric acids availability to

307 remove ammonia rapidly, hence causing an increase in lifetime.

308 **3.2 Satellite-constrained emissions**

309 The average ammonia emissions calculated from the 10-year IASI observations are

310 shown in **Figure 1**b (also in **Fig. S 1**a), the reactants' atmospheric burden in **Figure 1**c and their

311 seasonal variability in **Figure 1**d together with monthly modelled lifetimes. The year-by-year

312 total ammonia emissions are depicted in **Fig. S 1** with a monthly temporal resolution. Emissions

313 decline from 242 Tg yr^{-1} in 2008 to 212 Tg yr^{-1} in 2011. In 2012 – 2014, emissions show little

314 variation (194, 204 and 195 Tg yr^{-1}, respectively), before they increase steeply to 248 Tg yr^{-1}

315 in 2015. Finally, in 2016 and 2017 they remain at the same high level (197 and 227 Tg yr^{-1},

316 respectively).

317 The global average annual emission calculated from VD0.5 amounts to 189 Tg (9-year

318 average), which is comparable to the average of the 10-year period that we have calculated in

319 the present study (average±sd: 213±18.1 Tg yr^{-1}). The increase in the emissions we calculate

320 during 2015 and 2017 stand out. The explanation for these increases could be twofold: (i) if

321 sulfur dioxide (a precursor of sulfuric acid) emissions decreased over time, less sulfuric acid is

322 available to neutralize ammonia, hence resulting in higher ammonia column concentrations

323 seen by IASI that could be attributed to new emissions erroneously (see section 2.4); (ii) if

324 sulfur dioxide and sulfuric acid presented a constant year-by-year pattern or even increased,

325 then the calculated ammonia emissions would be likely real.

326 To sort out between these two possibilities, we used sulfur dioxide measurements from

327 NASA's Ozone Monitoring Instrument (OMI, Yang et al., 2007) instrument, whereas sulfate

column concentrations were taken from the Modern-Era Retrospective Analysis for Research and Applications, Version 2 (MERRA2, Gelaro et al., 2017) reanalysis data from NASA's Global Modeling and Assimilation Office (GMAO). Fig. S 2 shows timeseries of column concentrations of sulfur dioxide and sulfates from OMI and MERRA2 averaged globally, for continental regions (Europe, North America, South America, Africa), as well as for regions where ammonia emissions are particularly high (India and Southeastern Asia, North China Plain). Although column concentrations of both sulfur dioxide and sulfates present strong interannual variability (Fig. S 2), their global concentrations show a strong decreasing trend after 2015. The observed decrease indicates that sulfate amounts that neutralize ammonia and form ammonium sulfate, thus it is likely that the higher ammonia concentrations seen from IASI after 2015 are not necessarily a result of emission increases. This is not seen from the respective precursor of the atmospheric nitric acid, nitrogen dioxide (Fig. S 2). Sulfur dioxide emissions over Europe and North American have been reduced by 70–80% since 1990 (Vestreng et al., 2007). The largest emission reductions occurred in North America after 2005 (Hand et al., 2012; Hoesly et al., 2017; Lehmann et al., 2007; Sickles and Shadwick, 2015), while in Europe before 2000 (Crippa et al., 2016; Hoesly et al., 2017; Torseth et al., 2012; Vestreng et al., 2007). These large regional reductions of sulfur dioxide resulted in a global decrease until 2000, then slightly increased until 2006, due to a sharp rise in emissions in China, and declined again, due to stricter emission restriction in China (Klimont et al., 2013; Li et al., 2017, 2018; Saikawa et al., 2017a; Wang et al., 2017; Xing et al., 2015; Zhang et al., 2012; Zheng et al., 2018) and regulations in Europe and North America (Aas et al., 2019; Crippa et al., 2016; Hoesly et al., 2017; Klimont et al., 2013; Reis et al., 2012). This was not the case for India, where the emissions have been increasing (Hoesly et al., 2017; Klimont et al., 2017; Saikawa et al., 2017b) making it the world's second largest sulfur dioxide emitting country after China (Krotkov et al., 2016).

Looking closely into regions with large changes in ammonias reactants and/or their precursors after 2015 (Figure 2), we immediately see that a region of interest is the North China Plain. The North China Plain has been identified as an ammonia hotspot mainly due to extensive agricultural activities (Clarisse et al., 2009; Pan et al., 2018). To improve air quality over China, the Chinese government implemented new emission regulations aimed at decreasing the national total NO_x emissions by 10% between 2011 and 2015 (Liu et al., 2017). Several recent studies (Duncan et al., 2016; Krotkov et al., 2016) have highlighted the effectiveness of the air quality policy, as evidenced by a decreasing trend in nitrogen dioxide columns over China since

2012. De Foy et al. (2016) reported that NO_x reduction goals had already been achieved in 2016, as seen from satellites. A similar decreasing trend has been reported for sulfur dioxide (Koukouli et al., 2018; Krotkov et al., 2016; Wang et al., 2013). For instance, Liu et al. (2018) reported a sulfur dioxide reduction of about 60% over the recent few years in the North China Plain, sulfuric acid decreased by 50%, while ammonia emissions declined by only 7% due to change in agricultural practices.

The suggested decrease in ammonia reactants over the North China Plain is illustrated by the calculated sulfur dioxide column concentration anomaly from OMI (Figure 2) and by the sulfuric acid concentration anomaly from MERRA-2 after 2015 (the highest calculated one) (Fig. S 3). Nitrogen dioxide concentration do not show any noticeable annual change, despite their strong seasonal cycle (Fig. S 2). The IASI-constrained ammonia emissions calculated here show only a tiny increase of 0.19 ± 0.04 kt y^{-1} after 2015 in the North China Plain and of 10 ± 3.1 Tg y^{-1} globally with respect to the 10-year average (Figure 2). This is due to the change of sulfur dioxide and nitrogen oxide emission regulations in China, which in turn led to reduced inorganic matter (sulfates, nitrates and ammonium) resulting in regional increases of gaseous ammonia (Lachatre et al., 2019).

It should be noted here that decreases in sulfur dioxide and nitrogen dioxide have been reported to have occurred since 2005, at least in Eastern USA and to a lesser extent in Eastern Europe (Krotkov et al., 2016). At the same time, sulfur dioxide and nitrogen dioxide concentrations had started increasing after 2005 in India, a country that shows the largest agricultural activity in the world and is now the second largest sulfur dioxide emitting country after China (Krotkov et al., 2016). The latter has balanced the global sulfur dioxide and nitrogen dioxide budget, explaining that the decreasing trend after 2015 that we report has been affected by our choice to present global averages.

3.3 Comparison with traditional emission datasets

In this section, we quantify the main differences of our IASI-constrained emission dataset with other state-of-the-art inventories used in global models and for different applications (air quality, climate change etc...). Aside from comparing our emissions with those calculated using Van Damme et al. (2018) data with a constant lifetime (hereafter called VD0.5), we extend our comparison to more traditional datasets such as those of ECLIPSEv5-GFED4-GEIA (EGG) for 2008–2017, and EDGARv4.3.1-GFED4 (Crippa et al., 2016; Giglio et al., 2013) for 2008–2012 period. Finally, the ammonia emissions presented in this study (NE emissions) are compared

393 to emissions calculated from Van Damme et al. (2018) gridded IASI column data applying a

394 variable (modelled) ammonia lifetime presented in **Figure 1**b (hereafter referred as VDgrlf).

395 The 10-year comparison of our calculated emissions with VD0.5 is shown in **Figure 3**.

396 The 10-year average difference amounts to 29 ± 15 Tg yr^{-1} (average$\pm$sd). In all years, the largest

397 differences could be seen over Latin America and over tropical Africa. Our emissions (NE)

398 show a different structure in the Indo-Gangetic Plain and situated slightly more northerly than

399 those in VD0.5. The difference might be due to the IDW interpolation used to process the IASI

400 ammonia in the NE emissions compared with the oversampling method used in VD0.5 (see

401 section 2.3). Nevertheless, Northern India has been identified as a hot-spot region for ammonia,

402 mainly due the importance of agricultural activities in the region (Kuttippurath et al., 2020;

403 Tanvir et al., 2019).

404 **Fig. S 4** and **Fig. S 5** present a comparison of our calculated emissions (NE) with the basic

405 state-of-the-art datasets of EGG and EDGARv4.3.1-GFED4, respectively. In both datasets,

406 ammonia emissions remain almost constant over time (average$\pm$sd: 65 ± 2.8 Tg yr^{-1} and 103 ± 5.5

407 Tg yr^{-1}, respectively). The total calculated ammonia emissions in EGG and EDGARv4.3.1-

408 GFED4 are up to three times lower than those calculated from NE (average$\pm$sd: 213 ± 18.1 Tg

409 yr^{-1}) or from VD0.5 (9-year average: 189 Tg yr^{-1}). This results in 10-year annual differences

410 that are very significant (average$\pm$sd: 150 ± 19.3 Tg yr^{-1} and 111 ± 19.2 Tg yr^{-1}, respectively); the

411 largest differences appear over South America (EGG: 7.1 ± 0.3 Tg yr^{-1}, VD0.5: 22 Tg yr^{-1}, NE:

412 28 ± 3.0 Tg yr^{-1}, VDgrlf: 24 ± 1.3 Tg yr^{-1}), while European emissions are practically identical in

413 all datasets except EGG (EGG: 6.9 ± 1.1 Tg yr^{-1}, VD0.5: 11 Tg yr^{-1}, NE: 15 ± 2.2 Tg yr^{-1}, VDgrlf:

414 11 ± 1.0 Tg yr^{-1}). Emissions from South China Plain are much higher in the two traditional

415 datasets that those presented in this paper (EGG: 25 ± 1.2 Tg yr^{-1}, VD0.5: 36 Tg yr^{-1}, NE: 38 ± 2.8

416 Tg yr^{-1}, VDgrlf: 39 ± 1.8 Tg yr^{-1}). Ammonia emissions derived over China in this work (NE) are

417 among the highest worldwide (**Fig. S 1**), which agrees well with the 9-year average emissions

418 calculated in VD0.5 inventory over China (see **Figure 3**). To assess to which extent emissions

419 from EGG and EDGARv4.3.1-GFED4 are underestimated can only be done by comparing

420 ammonia with ground or satellite observations.

421 The comparison of the annual ammonia emissions in the NE dataset to the modified

422 VDgrlf emissions is shown in **Fig. S 6**. The latter showed a better agreement to the emissions

423 presented in this study with mean annual different of 14 ± 19 Tg yr^{-1} (average$\pm$sd). Previously

observed emission differences in the two state-of-the-art inventories over South America and Africa have been now minimized, as well as the displacement north of the Indo-Gangetic Plain emissions remains important. Nevertheless, the smaller differences of our emissions (NE) from those of VDgrlf as compared with the respective difference from the VD0.5 emissions, show the large impact that a more realistic variable lifetime might have in emission calculations with this methodology in these regions.

3.4 Region-specific ammonia emissions and seasonal variation

Figure 4 illustrates specific regions that show the largest ammonia emissions (Europe, North America, South America and Southeastern Asia). These emissions correspond to the IASI-constrained emissions calculated in this study (NE) and are presented as total annual emissions averaged over the 10-year period of study. At the bottom panels of the same figure, the seasonal variation of the emissions is shown for each of the four hot-spot regions and each of the 10 years of the study.

European total ammonia emissions were estimated to be 15 ± 2.2 Tg yr^{-1} (average±sd), more than double compared with those reported in EGG (6.9 ± 1.1 Tg yr^{-1}) and similar to those in VD0.5 (11 Tg yr^{-1}) or those in VDgrlf (11 ± 1.0 Tg yr^{-1}). The greatest emissions were calculated for Belgium, the Netherlands and the Po Valley in Italy (Figure 4). High emissions are also found in North and Northwestern Germany and over Denmark. In contrast, very low emissions are found in Norway, Sweden and parts of the Alps. It is not possible to quantitatively distinguish between different sources of ammonia. It has been reported that approximately 75% of ammonia emissions in Europe originate from livestock production (Webb et al., 2005), and 90% from agriculture in general (Leip et al., 2015). More specifically, ammonia is emitted from all stages of manure management, from livestock buildings during manure storage and application to land, as well as from livestock urine. These emissions are strong over most of Northwestern European countries, although sources like fertilization and non-agricultural activities (traffic and urban emissions) can be also important. An example is Tange in Germany, which shows a late summer peak due to growing crops application. No obvious seasonality in the emissions can be seen for Europe as a whole, as the hot-spot regions are rather few compared to the overall surface of Europe. An exception to this stable emission situation over the year occurs during 2010 and during 2015, years for which a late summer peak. In 2010, large wildfires in Russia resulted in high ammonia emissions (R'Honi et al., 2013), while year 2015

has been also characterized as an intense fire year (though not like 2010), with fires occurring in Eurasia (Min Hao et al., 2016).

North America and in particular the US (Figure 4) has been characterized by four hot-spot regions. First, a small region in Colorado, Central US, which is the location of a large agricultural region that traditionally releases large ammonia emissions (Malm et al., 2013). Another example is the state of Iowa (home to more than 20 million swine, 54 million chickens, and 4 million cattle), northern Texas and Kansas (beef cattle), and southern Idaho (dairy cattle) (McQuilling, 2016). Furthermore, the three major valleys in Salt Lake, in Cache, and in Utah in the midwestern US show an evident, but lower intensity hot-spot, as they are occupied by massive pig farms associated to open waste pits. The largest emissions were calculated for the San Joaquin Valley in California (vegetables, dairy, beef cattle and chickens) and further to the South (Tulare and Bakersfield), an area characterized by feedlots (Van Damme et al., 2018; McQuilling, 2016). North American annual ammonia emissions over the 10-year period were averaged 1.1 ± 0.1 Tg yr^{-1} (average±sd). These values are over two orders of magnitude higher than those in EGG (0.062 ± 0.0013 Tg yr^{-1}). Note that his estimate is three times lower than those reported in VD0.5 (3.1 Tg yr^{-1}) or in VDgrlf (3.4 ± 0.5 Tg yr^{-1}). The 2008–2017 interannual variability (Figure 4) all show a minimum in winter. Maximum emissions were observed in late spring, due to the contribution from mineral fertilizer and manure application, in summer, due to influence of livestock housing emissions, and some years both in spring and summer (Makar et al., 2009; Zhu et al., 2013, 2015). A topographical dependence was also seen in midwest emissions that peaked in April, whereas over the rest of the US maximum emissions were appeared in summer (Paulot et al., 2014).

Ammonia emissions have different characteristics in South America and in Western Africa as both are fire-dominated regions. For simplicity we only present South America in Figure 4. This region is dominated by natural ammonia emissions mainly from forest, savanna and agricultural fires (Whitburn et al., 2014, 2016b) and volcanoes (Kajino et al., 2004; Uematsu et al., 2004). This causes a strong seasonal variability in the ammonia emissions with the largest fluxes observed from August to October in all years (Figure 4). This strong dependence of South America from biomass burning emissions was first highlighted by Chen et al. (2013) and by van Marle et al. (2017). It also became particularly pronounced during the large wildfires in the Amazon rainforest in summer 2019 (Escobar, 2019). We estimated the 10-year average ammonia emissions to be 28 ± 3.0 Tg yr^{-1} (average±sd) in agreement with

487   VD0.5 (22 Tg yr^{-1}) and VDgrlf (24±1.3 Tg yr^{-1}). The respective emissions in EGG are four

488   times lower than these estimates (7.1±0.3 Tg yr^{-1}).

489   The last column to the right of **Figure 4** presents the 10-year average annual ammonia

490   emissions and their respective interannual variability in Southeastern Asia. We define this

491   region spanning from 70°E–130°E in longitude and from 0°N–45°N in latitude. Ammonia

492   emissions were estimated to be 38±2.8 Tg yr^{-1} (average±sd) similar to VD0.5 (36 Tg yr^{-1}) and

493   VDgrlf (39±1.8 Tg yr^{-1}) and slightly higher than those presented in EGG (25±1.2 Tg yr^{-1}). They

494   comprise ammonia fertilizer plants, such as in Pingsongxiang, Shizuishan, Zezhou-Gaoping,

495   Chaerhan Salt Lake, Delingha, Midong-Fukang and Wucaiwan (China), Indo-Gangetic Plain

496   (Pakistan and India), Gresik (Indonesia). China and India contribute more than half of total

497   global ammonia emissions since the 1980s with the majority of these emissions to originate

498   from rice cultivation followed by corn and wheat (crop-specific emissions). More specifically,

499   emissions from these crops due to synthetic fertilizer and livestock manure applications are

500   concentrated in North China Plain (Xu et al., 2018). Considering that Southeastern Asia is the

501   largest agricultural contributor in the global ammonia budget, a strong seasonality in the

502   emissions was observed. Temporal ammonia emissions peak in late summer of most years,

503   when emissions from rice cultivation, synthetic fertilizer application and livestock manure

504   spreading (Xu et al., 2016) are important, and in spring when wheat cultivation dominates

505   (Datta et al., 2012). Of course, the respective emissions from biomass burning should also be

506   mentioned. However, these are difficult to be distinguish and are expected to be a relatively

507   small source compared to agricultural emissions.

4 Discussion

509   In this section, we conduct simulations over the 10-year period (2008–2017, 1-year spin-

510   up), with all the emissions derived and compare the NH$_3$ concentrations with ground-based

511   observations over Europe, North America, Southeastern Asia (section 4.1), and observations

512   from CrIS (section 4.1). These simulations consist in: (i) a simulation using traditional

513   emissions using EGG; (ii) a simulation using emissions calculated from IASI data from Van

514   Damme et al. (2018) applying a constant lifetime of 12 hours for ammonia (VD0.5); (iii) a

515   simulation using gridded emissions presented in the present paper (NE) calculated as described

516   in section 2; and (iv) a simulation using emissions calculated from IASI data from Van Damme

517   et al. (2018) applying a variable (modelled) lifetime (VDgrlf). Finally, we perform a sensitivity

analysis in order to define the levels of uncertainty of our emissions in section 4.2 and discuss potential limitation of the present study in section 4.3.

4.1 Validation against ground-based observations and satellite products

Figure 5 shows a comparison between modelled surface concentrations of ammonia with ground measurements from Europe (EMEP, https://emep.int/mscw/), North America (AMoN, http://nadp.slh.wisc.edu/data/AMoN/) and Southeastern Asia (EANET, https://www.eanet.asia). To avoid overplotting, the Gaussian kernel density estimation (KDE) was used, which is a non-parametric way to estimate the probability density function (PDF) of a random variable (Parzen, 1962):

$$f(x) = \frac{1}{Nh} \sum_{i=1}^{N} K(\frac{x-x_i}{h}) \qquad \textbf{Eq. 7}$$

where K is the kernel, x_i the univariate independent and identically distributed point of the relationship between modelled and measured ammonia and h is a smoothing parameter called the bandwidth. KDE is a fundamental data smoothing tool that attempts to infer characteristics of a population, based on a finite dataset. It weighs the distance of all points in each specific location along the distribution. If there are more points grouped locally, the estimation is higher as the probability of seeing a point at that location increases. The kernel function is the specific mechanism used to weigh the points across the data set and it uses the bandwidth to limit the scope of the function. The latter is computed using the Scott's factor (Scott, 2015). We also provide the mean fractional bias (MFB) for modelled and measured concentrations of ammonia as follows:

$$MFB = \frac{1}{N} \frac{\sum_{i=1}^{N}(C_m - C_o)}{\sum_{i=1}^{N}(\frac{C_m + C_o}{2})} \times 100\% \qquad \textbf{Eq. 8}$$

where C_m and C_o are the modelled and measured ammonia concentrations and N is the total number of observations. MFB is a symmetric performance indicator that gives equal weights to under- or over-estimated concentrations (minimum to maximum values range from -200% to 200%). Furthermore, we assess the deviation of the data from the line of best fit using the root mean square error (RMSE) defined as:

$$RMSE = \sqrt{\sum_{i=1}^{N} \frac{(C_m - C_o)^2}{N}} \qquad \textbf{Eq. 9}$$

From 134 European stations, nearly 300,000 measurements made at a daily to weekly temporal resolution over the period of study (2007–2018) are presented on **Figure 5**. All emission datasets underestimate ammonia surface concentration over Europe. The most accurate prediction of concentrations was achieved using the traditional EGG emissions that

underestimated observations by 67%, also being the least scattered from the best fit ($RMSE_{EGG} = 4.06\,\mu g\,N\,m^{-3}$), followed by the emissions presented in this paper ($MFB_{NE} = -72\%$, $RMSE_{NE} = 4.65\,\mu g\,N\,m^{-3}$), although they were more variable. VD0.5 or VDgrlf emissions further underestimated observations, though they were less sparse (**Figure 5**d). About 12% of the modelled concentrations using EGG were outside of the 10-fold limit from the observations, in contrast to only 17% and 15% in VD0.5 and VDgrlt, and 20% in NE. With regards to the spatial comparison with the observed concentrations, all datasets cause overestimations in the ammonia concentrations predicted in Western Europe. EGG appears to be the most accurate in Central Europe (all stations with suffix DE00), NE emissions in all Spanish stations (suffix ES00) and VD0.5 and VDgrlf emissions in Italian stations (**Fig. S 7**).

The comparison of simulated ammonia concentrations to observations over North America includes 119 stations, which represent nearly 27,000 observations (Figure 6) with a weekly, bi-weekly or monthly resolution. The only emission dataset that lead to an underestimation of ammonia concentrations was EGG ($\mathbf{MFB_{EGG} = -28\%}$). Two others, VD0.5 and VDgrlf caused ammonia observations to be strongly overestimated ($\mathbf{MFB_{VD0.5} = 52\%}$ $\boldsymbol{and}$ $\mathbf{MFB_{VDgrlf} = 54\%}$), while NE slightly ($\mathbf{MFB_{NE} = 32\%}$). All inventories resulted in about the same variability in ammonia concentrations with RMSEs between 4.15 and 4.17 μg N m-3 (Figure 6). About 10% of the predicted concentrations using EGG emissions were at least 10 times off from the measured ones, more than twice the number of measurements compared to the other dataset. NE emissions better capture levels in the easternmost stations of the US (AL99, AR15, CT15, IL37, IN22, MI52, NY56, ON26) and in California (CA83) and Oklahoma (OK98), which are close to hot-spot regions (see section 3.4). EGG emissions perform better in Northwestern (ID03), Central (KS03) and several stations located over the Eastern United States (KY03, KY98, OH09, AR03, IL46, KS03, GA41). The emission inventory VD0.5 leads to a very good agreement in ammonia concentrations over all stations of the North American continent (AL99, GA40, ID03, GA41, IL37, IL46, IN20, IN22, KS97, PA00, MD99, MI52, TN04, NM99, NY96, OH99, OK98) (Fig. S 8).

In Southeastern Asia 62 stations from 13 countries were included in the comparison from the EANET monitoring network (**Figure 7**). These included about 8,000 surface measurements in monthly or 2-weekly resolution. As a whole, all emission inventories underestimate station concentrations of EANET with MFBs between -102% (EGG) and -61% (VD0.5 and VDgrlf). The least spread model concentrations were those simulated using VD0.5 and VDgrlf

581 ($\boldsymbol{RMSE = 4.61 - 4.65\,\mu g\,N\,m^{-3}}$). Around 19% of model concentrations using EGG were

582 outside the 10-fold limit of the 1×1 line with observations, 12% using NE emissions and only

583 5% and 6% using VD0.5 and VDgrlf, respectively. VD0.5 and VDgrlf emissions capture well

584 the Japanese (suffix JPA) and Taiwanese stations (suffix THA). Given the short lifetime and

585 the relatively coarse spatial scales, the model fails to capture the variability that exists within

586 each gridbox (Fig. S **9**).

587   To give an overview of the comparison of the modelled surface concentrations of

588 ammonia from the four different simulations, each with different emissions (EGG, VD0.5, NE

589 and VDgrlf), we present station-by-station calculated MFB values in **Figure 8**. Although the

590 traditional EGG emissions capture many stations very well, there are large MFB values

591 observed in Eastern and Western USA (AMoN), Northern Europe (EMEP), whereas large

592 overestimations are observed in most of the Southeastern Asian stations (EANET). The large

593 bias at several AMoN stations decrease when using satellite-derived emissions. All datasets

594 miscalculated surface concentrations in Southeastern Asia, although some stations present

595 lower MFBs when using IASI constrained emissions. Note that large differences when

596 comparing bias from all measurements versus station-by-station bias have been calculated as a

597 result of the different frequency of measurements in each station.

598   To further show whether the satellite-derived emissions presented here (NE) capture

599 surface concentrations of ammonia or not, we used surface ammonia concentrations from CrIS

600 from 1st May 2012 to 31st December 2017. The comparison is shown as PDF of surface

601 modelled against CrIS concentrations of ammonia calculated with the Gaussian KDE for North

602 America, Europe and Southeastern Asia in **Figure 9**. NE emissions slightly overestimate

603 ammonia ($MFB = 0.09 - 0.10$). NE emissions generally result in higher surface

604 concentrations, also showing large $RMSEs$ (3.28 – 5.26 µg N m^{-3}). However, 90% of the

605 modelled concentrations were within a factor of 10 from the CrIS observation. .

4.2 Uncertainty analysis

607   A sensitivity analysis in order to calculate the level of uncertainty that each of the

608 parameter gives to the modelled surface concentrations of ammonia was also performed. The

609 relative uncertainty was calculated as the standard deviation of ammonia's surface

610 concentrations from a model ensemble of 10 members (**Table 1**) divided by the average. The

611 first six members are the surface concentrations that resulted from simulations of ammonia

612 emissions after perturbation of the Euclidian distance d_k in the parameters of the IDW

613 interpolation. The remaining four members are simulated concentrations using the previously

614 reported emissions datasets (EGG, VD0.5, NE and VDgrlf). The results are shown as a 10-year

615 (2008–2017) annual average relative uncertainty in **Figure 10** and as annual average relative

616 uncertainty of surface concentrations for every year of the 10-year period in Fig. S 10.

617   The surface concentrations resulting from the different calculated emissions mainly

618 affects oceanic regions, with values reaching 100%. The reason for this could be threefold.

619 First, the IDW interpolation shows to be affected by severe outlier values, which are found in

620 several oceanic regions (Fig. S 11); this creates high gridded column ammonia concentrations

621 and, in turn, fluxes at regions that are not supported by previous findings or measurements.

622 Second, the methodology with which ammonia concentrations are retrieved in IASI has certain

623 limitation, with respect to (i) the use of constant vertical profiles for ammonia, (ii) potential

624 dependencies of total column ammonia and temperature that are not taken into account, and

625 (iii) instrumental noise that can cause bias (Whitburn et al., 2016a). Third, there is much less

626 ammonia over the Ocean, hence the relative error bars are much larger. Large uncertainties in

627 surface ammonia concentrations were observed in regions characterized by large anthropogenic

628 contribution, such as North India, North China Plain and Central USA. Smaller uncertainties

629 were found in Central Africa and in Amazonia, regions that are linked with episodic biomass

630 burning emissions (**Figure 4**).

4.3   Limitations of the present study

631

632   We discuss the importance of certain limitations in the methodology of the present study

633 and in the validation of the results. These limitations will also be commented upon in the overall

634 conclusion of the paper.

635   Regarding the methodology, emissions of short-lived species are determined, among

636 other methods, using top-down approaches. When only satellite measurements are available,

637 they are usually averaged over a particular location and surface emissions are calculated using

638 a mass balance approach (Lin et al., 2010; Zhao and Wang, 2009). This is done by assuming a

639 1-dimensional box-model, where atmospheric transport between grids is assumed to be

640 negligible and loss due to deposition or chemical reactions very fast. The solution to this

641 problem is the use of Kernels (Boersma et al., 2008), which makes the computation of the

642 emissions very intense. It has been reported that for resolutions, such as those used in the

643 present paper (2.5°×1.3°), non-local contributions to the ammonia emissions are relatively

644 small (Turner et al., 2012). Although, the use of Kernels is the proper way to account for non-

645 local contributions, we believe that negligible transport here is a fair assumption, due to the

646 small lifetimes of ammonia calculated from the CTM (11.6±0.6 hours); therefore,

647 transportation from the adjacent grid-cells should be small. Note that although this method has

648 been suggested for short lived climate pollutants, it is not suitable for species with lifetime from

649 days to weeks (e.g. black carbon, Bond et al., 2013). Another important process that is not yet

650 considered in our model is the treatment of ammonia's air-surface exchange. Although bi-

651 directional air-surface exchange (dry deposition and emission) of ammonia has been observed

652 over a variety of land surfaces (grasslands, tree canopies etc…), the majority of the CTMs treats

653 the air-surface exchange of ammonia as dry deposition only. This might cause underestimation

654 of the daytime ambient ammonia concentration due to the overestimated dry deposition,

655 considering that the observed bi-directional exchange of ammonia mainly occurs during the

656 daytime (see Zhang et al., 2010, and references therein).

657   Another limitation of the present study is that the same model is used for the calculation

658 of the modelled lifetimes and for the validation of the emissions that were calculated using

659 these lifetimes (NE and VDgrlf). A more accurate validation would require an independent

660 model for the simulations of surface concentrations using these emissions. Nevertheless, the

661 IASI-constrained emissions of ammonia presented here are publicly available for use in global

662 models.

5 Conclusions

664   In the present paper, satellite measurements from IASI were used to constrain global

665 ammonia emissions over the period 2008–2017. The data were firstly processed to monthly

666 ammonia column concentrations with a spatial resolution of 2.5°×1.3°. Then, using gridded

667 lifetime for ammonia calculated with a CTM, monthly fluxes were derived. This contrasts with

668 previously reported methods that used a single constant lifetime. This enables a more accurate

669 calculation in regions where different abundances of atmospheric sulfuric and nitric acid, as

670 well as in their precursors (sulfur and nitrogen dioxide, respectively) can neutralize ammonia

671 through heterogeneous chemical reactions to sulfate and nitrate aerosols. The calculated

672 ammonia emission fluxes were then used to simulate ammonia concentrations for the period

673 2008–2017 (referred to as NE). The same simulations were repeated using baseline emissions

674 from ECLIPSEv5-GFED4-GEIA (referred to as EGG), emissions constrained by Van Damme

675 et al. (2018) IASI data using a constant lifetime for ammonia (named as VD0.5) and emissions

676 based on Van Damme et al. (2018) retrievals using a modelled lifetime from a CTM (named as

VDgrlf). The simulated surface concentrations of ammonia were compared with ground measurements over Europe (EMEP), North America (AMoN) and Southeastern Asia (EANET), as well as with global satellite measurements from CrIS. The main conclusions can be summarized as follows:

- The 10-year average annual ammonia emissions calculated here (NE) were estimated to be 213±18.1 Tg yr^{-1}, which is 15% higher than those in VD0.5 (189 Tg yr^{-1}), and 6% higher than those in VDglrf (201±10.4 Tg yr^{-1}). These emission values amount to twice the published from datasets, such as EGG (65±2.8 Tg yr^{-1}) and EDGARv4.3.1-GFED4, (103±5.5 Tg yr^{-1}).

- In the North China Plain, a region characterized by intensive agricultural activities, a small increase of ammonia emissions is simulated after 2015. This is attributed to decreases in sulfur species, as revealed from OMI and MERRA-2 measurements. Less sulfates in the atmosphere leads to less ammonia neutralization and hence to larger loads in the atmospheric column as measured by IASI.

- In Europe, the 10-year average of ammonia emissions were estimated at 15±2.2 Tg yr^{-1} (NE), twice as much as those in EGG (6.9±1.1 Tg yr^{-1}) and similar to those in VD0.5 (11 Tg yr^{-1}) or VDgrlf (11±1.0 Tg yr^{-1}). The strongest emission fluxes were calculated over Belgium, Netherlands, Italy (Po Valley), Northwestern Germany and Denmark. These regions are known for industrial and agricultural applications, animal breeding activities, manure/slurry storage facilities and manure/slurry application to soils.

- Some hot-spot regions with high ammonia emissions were distinguished in North America: (i) in Colorado, due to large agricultural activity, (ii) in Iowa, northern Texas and Kansas, due to animal breeding, (iii) in Salt Lake, Cache, and Utah, due to animal farms associated with open waste pits and (iv) in California, due to animal breeding and agricultural practices. Ammonia emissions in North America were 1.1±0.1 Tg yr^{-1} or two orders of magnitude higher than in EGG (6.2±0.1 kt yr^{-1}) and three times lower than those in VD0.5 (3.1 Tg yr^{-1}) or in VDgrlf (3.4±0.5 Tg yr^{-1}), with maxima observed in late spring, due to fertilization and manure application and summer, due to livestock emissions.

- South America is dominated by natural ammonia emissions mainly from forest, savanna and agricultural fires causing a strong seasonality with the largest fluxes between August and October. The 10-year average ammonia emissions were as high as 28±3.0 Tg yr^{-1} similar to VD0.5 (22 Tg yr^{-1}) and VDgrlf (24±1.3 Tg yr^{-1}) and four times higher than EGG (7.1±0.3 Tg yr^{-1}).

710 • In Southeastern Asia, the 10-year average ammonia emissions were 38±2.8 Tg yr^{-1}, in

711 agreement with VD0.5 (36 Tg yr^{-1}) and VDgrlf (39±1.8 Tg yr^{-1}) and slightly higher than

712 those in EGG (25±1.2 Tg yr^{-1}). The main sources were from fertilizer plants in China,

713 Pakistan, India and Indonesia. China and India hold the largest share in the ammonia

714 emissions mainly due to rice, corn and wheat cultivation. A strong seasonality in the

715 emissions was observed with a late summer peak in most years, due to rice cultivation,

716 synthetic fertilizer and livestock manure applications and in spring due to wheat

717 cultivation.

718 • Large bias was calculated in several ground-based stations when using the state-of-the-art

719 emissions EGG. The bias decreased substantially when satellite-derived emissions were

720 used to simulate surface concentrations of ammonia.

721

722 *Data availability.* All data and python scripts used for the present publication are open through

723 the web address https://folk.nilu.no/~nikolaos/acp-2020-1008/ or can be obtained from the

724 corresponding author upon request.

725

726 *Competing interests.* The authors declare no competing interests.

727

728 *Acknowledgements.* We thank Espen Sollum for his continuous contribution and help with

729 big data analysis.

730

731 *Financial support.* This study was supported by the Research Council of Norway (project ID:

732 275407, COMBAT – Quantification of Global Ammonia Sources constrained by a Bayesian

733 Inversion Technique). Lieven Clarisse and Martin Van Damme are supported by the F.R.S.–

734 FNRS.

735

736 *Author contributions.* N.E. performed the simulations, analyses, wrote and coordinated the

737 paper. S.E. contributed to the lifetime calculations. Y.B., D.H. and A.C. set up the CTM model.

738 M.V.D., P.-F.C. and L.C. provided the IASI data, while M.W.S. and K.E.C.-P. provided the

739 observations from CrIS. All authors contributed to the final version of the manuscript.

740

741 **References**

742 Aas, W., Mortier, A., Bowersox, V., Cherian, R., Faluvegi, G., Fagerli, H., Hand, J.,

743 Klimont, Z., Galy-Lacaux, C., Lehmann, C. M. B., Myhre, C. L., Myhre, G., Olivié, D.,

744 Sato, K., Quaas, J., Rao, P. S. P., Schulz, M., Shindell, D., Skeie, R. B., Stein, A.,

Takemura, T., Tsyro, S., Vet, R. and Xu, X.: Global and regional trends of atmospheric sulfur, Sci. Rep., 9(1), 1–11, doi:10.1038/s41598-018-37304-0, 2019.

Abbatt, J. P. D., Benz, S., Cziczo, D. J., Kanji, Z., Lohmann, U. and Mohler, O.: Solid Ammonium Sulfate Aerosols as Ice Nuclei: A Pathway for Cirrus Cloud Formation, Science (80-.)., (September), 1770–1773, 2006.

Anderson, N., Strader, R. and Davidson, C.: Airborne reduced nitrogen: Ammonia emissions from agriculture and other sources, Environ. Int., 29(2–3), 277–286, doi:10.1016/S0160-4120(02)00186-1, 2003.

Aneja, V. P., Schlesinger, W. H. and Erisman, J. W.: Farming pollution, Nat. Geosci, 1(7), 409–411 [online] Available from: http://dx.doi.org/10.1038/ngeo236, 2008.

Aneja, V. P., Schlesinger, W. H. and Erisman, J. W.: Effects of agriculture upon the air quality and climate: Research, policy, and regulations, Environ. Sci. Technol., 43(12), 4234–4240, doi:10.1021/es8024403, 2009.

August, T., Klaes, D., Schlüssel, P., Hultberg, T., Crapeau, M., Arriaga, A., O'Carroll, A., Coppens, D., Munro, R. and Calbet, X.: IASI on Metop-A: Operational Level 2 retrievals after five years in orbit, J. Quant. Spectrosc. Radiat. Transf., 113(11), 1340–1371, doi:10.1016/j.jqsrt.2012.02.028, 2012.

Behera, S. N., Sharma, M., Aneja, V. P. and Balasubramanian, R.: Ammonia in the atmosphere: A review on emission sources, atmospheric chemistry and deposition on terrestrial bodies, Environ. Sci. Pollut. Res., 20(11), 8092–8131, doi:10.1007/s11356-013-2051-9, 2013.

Boersma, K. F., Jacob, D. J., Bucsela, E. J., Perring, A. E., Dirksen, R., van der A, R. J., Yantosca, R. M., Park, R. J., Wenig, M. O., Bertram, T. H. and Cohen, R. C.: Validation of OMI tropospheric NO2 observations during INTEX-B and application to constrain NOx emissions over the eastern United States and Mexico, Atmos. Environ., 42(19), 4480–4497, doi:10.1016/j.atmosenv.2008.02.004, 2008.

Bond, T. C., Doherty, S. J., Fahey, D. W., Forster, P. M., Berntsen, T., Deangelo, B. J., Flanner, M. G., Ghan, S., Kärcher, B., Koch, D., Kinne, S., Kondo, Y., Quinn, P. K., Sarofim, M. C., Schultz, M. G., Schulz, M., Venkataraman, C., Zhang, H., Zhang, S., Bellouin, N., Guttikunda, S. K., Hopke, P. K., Jacobson, M. Z., Kaiser, J. W., Klimont, Z., Lohmann, U., Schwarz, J. P., Shindell, D., Storelvmo, T., Warren, S. G. and Zender, C. S.: Bounding the role of black carbon in the climate system: A scientific assessment, J. Geophys. Res. Atmos., 118(11), 5380–5552, doi:10.1002/jgrd.50171, 2013.

Bouwman, A. F., Lee, D. S., Asman, W. A. H., Dentener, F. J., Van Der Hoek, K. W. and Olivier, J. G. J.: A global high-resolution emission inventory for ammonia, Global Biogeochem. Cycles, 11(4), 561–587, doi:10.1029/97GB02266, 1997.

Cao, H., Henze, D. K., Shephard, M. W., Dammers, E., Cady-Pereira, K., Alvarado, M., Lonsdale, C., Luo, G., Yu, F., Zhu, L., Danielson, C. G. and Edgerton, E. S.: Inverse modeling of NH3 sources using CrIS remote sensing measurements, Environ. Res. Lett., in press, doi:10.1088/1748-9326/abb5cc, 2020.

Chen, Y., Morton, D. C., Jin, Y., Gollatz, G. J., Kasibhatla, P. S., Van Der Werf, G. R., Defries, R. S. and Randerson, J. T.: Long-term trends and interannual variability of forest, savanna and agricultural fires in South America, Carbon Manag., 4(6), 617–638, doi:10.4155/cmt.13.61, 2013.

Clarisse, L., Clerbaux, C., Dentener, F., Hurtmans, D. and Coheur, P.-F.: Global ammonia distribution derived from infrared satellite observations, Nat. Geosci, 2(7), 479–483 [online] Available from: http://dx.doi.org/10.1038/ngeo551, 2009.

Clarisse, L., Shephard, M. W., Dentener, F., Hurtmans, D., Cady-Pereira, K., Karagulian, F., Van Damme, M., Clerbaux, C. and Coheur, P. F.: Satellite monitoring

795   of ammonia: A case study of the San Joaquin Valley, J. Geophys. Res., 115,
796   doi:10.1029/2009jd013291, 2010.
797   Clerbaux, C., Boynard, A., Clarisse, L., George, M., Hadji-Lazaro, J., Herbin, H.,
798   Hurtmans, D., Pommier, M., Razavi, A., Turquety, S., Wespes, C. and Coheur, P.-F.:
799   Monitoring of atmospheric composition using the thermal infrared IASI/MetOp
800   sounder, Atmos. Chem. Phys., 9(16), 6041–6054, doi:10.5194/acp-9-6041-2009,
801   2009.
802   De Cort, M., Dubois, G., Fridman, S. D., Germenchuk, M., G., Izrael, Y. A., Janssens,
803   A., Jones, A. R., Kelly, G., N., Kvasnikova, E., V., Matveenko, I., I., Nazarov, I., N.,
804   Pokumeiko, Y., M., Sitak, V. A., Stukin, E., D., Tabachny, L., Y., Tsaturov, Y. S. and
805   Avdyushin, S., I.: Atlas of caesium deposition on Europe after the Chernobyl
806   accident, EU - Office for Official Publications of the European Communities,
807   Luxembourg., 1998.
808   Crippa, M., Janssens-Maenhout, G., Dentener, F., Guizzardi, D., Sindelarova, K.,
809   Muntean, M., Van Dingenen, R. and Granier, C.: Forty years of improvements in
810   European air quality: Regional policy-industry interactions with global impacts,
811   Atmos. Chem. Phys., 16(6), 3825–3841, doi:10.5194/acp-16-3825-2016, 2016.
812   Croft, B., Pierce, J. R. and Martin, R. V.: Interpreting aerosol lifetimes using the
813   GEOS-Chem model and constraints from radionuclide measurements, Atmos. Chem.
814   Phys., 14(8), 4313–4325, doi:10.5194/acp-14-4313-2014, 2014.
815   Van Damme, M., Wichink Kruit, R. J., Schaap, M., Clarisse, L., Clerbaux, C., Coheur,
816   P. F., Dammers, E., Dolman, A. J. and Erisman, J. W.: Evaluating 4 years of
817   atmospheric ammonia (NH3) over Europe using IASI satellite observations and
818   LOTOS-EUROS model results, J. Geophys. Res. Atmos., 119(15), 9549–9566,
819   doi:10.1002/2014JD021911, 2014a.
820   Van Damme, M., Clarisse, L., Heald, C. L., Hurtmans, D., Ngadi, Y., Clerbaux, C.,
821   Dolman, A. J., Erisman, J. W. and Coheur, P. F.: Global distributions, time series and
822   error characterization of atmospheric ammonia (NH3) from IASI satellite
823   observations, Atmos. Chem. Phys., 14(6), 2905–2922, doi:10.5194/acp-14-2905-
824   2014, 2014b.
825   Van Damme, M., Clarisse, L., Dammers, E., Liu, X., Nowak, J. B., Clerbaux, C.,
826   Flechard, C. R., Galy-Lacaux, C., Xu, W., Neuman, J. A., Tang, Y. S., Sutton, M. A.,
827   Erisman, J. W. and Coheur, P. F.: Towards validation of ammonia (NH3)
828   measurements from the IASI satellite, Atmos. Meas. Tech., 8(3), 1575–1591,
829   doi:10.5194/amt-8-1575-2015, 2015.
830   Van Damme, M., Whitburn, S., Clarisse, L., Clerbaux, C., Hurtmans, D. and Coheur,
831   P.: Version 2 of the IASI NH 3 neural network retrieval algorithm : near-real-time and
832   reanalysed datasets, , 4905–4914, 2017.
833   Van Damme, M., Clarisse, L., Whitburn, S., Hadji-Lazaro, J., Hurtmans, D., Clerbaux,
834   C. and Coheur, P.-F.: Industrial and agricultural ammonia point sources exposed,
835   Nature, 564(7734), 99–103, doi:10.1038/s41586-018-0747-1, 2018.
836   Dammers, E., Palm, M., Van Damme, M., Vigouroux, C., Smale, D., Conway, S.,
837   Toon, G. C., Jones, N., Nussbaumer, E., Warneke, T., Petri, C., Clarisse, L.,
838   Clerbaux, C., Hermans, C., Lutsch, E., Strong, K., Hannigan, J. W., Nakajima, H.,
839   Morino, I., Herrera, B., Stremme, W., Grutter, M., Schaap, M., Kruit, R. J. W., Notholt,
840   J., Coheur, P. F. and Erisman, J. W.: An evaluation of IASI-NH 3 with ground-based
841   Fourier transform infrared spectroscopy measurements, Atmos. Chem. Phys.,
842   16(16), 10351–10368, doi:10.5194/acp-16-10351-2016, 2016.
843   Dammers, E., Shephard, M. W., Palm, M., Cady-pereira, K., Capps, S., Lutsch, E.,
844   Strong, K., Hannigan, J. W., Ortega, I., Toon, G. C., Stremme, W. and Grutter, M.:

845   Validation of the CrIS fast physical NH 3 retrieval with ground-based FTIR, , 87,
846   2645–2667, 2017.
847   Dammers, E., McLinden, C. A., Griffin, D., Shephard, M. W., Van Der Graaf, S.,
848   Lutsch, E., Schaap, M., Gainairu-Matz, Y., Fioletov, V., Van Damme, M., Whitburn,
849   S., Clarisse, L., Cady-Pereira, K., Clerbaux, C., Francois Coheur, P. and Erisman, J.
850   W.: NH3 emissions from large point sources derived from CrIS and IASI satellite
851   observations, Atmos. Chem. Phys., 19(19), 12261–12293, doi:10.5194/acp-19-
852   12261-2019, 2019.
853   Datta, A., Sharma, S. K., Harit, R. C., Kumar, V., Mandal, T. K. and Pathak, H.:
854   Ammonia emission from subtropical crop land area in india, Asia-Pacific J. Atmos.
855   Sci., 48(3), 275–281, doi:10.1007/s13143-012-0027-1, 2012.
856   Dee, D. P., Uppala, S. M., Simmons, A. J., Berrisford, P., Poli, P., Kobayashi, S.,
857   Andrae, U., Balmaseda, M. A., Balsamo, G., Bauer, P., Bechtold, P., Beljaars, A. C.
858   M., van de Berg, L., Bidlot, J., Bormann, N., Delsol, C., Dragani, R., Fuentes, M.,
859   Geer, A. J., Haimberger, L., Healy, S. B., Hersbach, H., H??lm, E. V., Isaksen, L.,
860   K??llberg, P., K??hler, M., Matricardi, M., Mcnally, A. P., Monge-Sanz, B. M.,
861   Morcrette, J. J., Park, B. K., Peubey, C., de Rosnay, P., Tavolato, C., Th??paut, J. N.
862   and Vitart, F.: The ERA-Interim reanalysis: Configuration and performance of the
863   data assimilation system, Q. J. R. Meteorol. Soc., 137(656), 553–597,
864   doi:10.1002/qj.828, 2011.
865   Dentener, F. J. and Crutzen, P. J.: A 3-Dimensional Model Of The Global Ammonia
866   Cycle, J. Atmos. Chem., 19(4), 331–369, doi:10.1007/bf00694492, 1994.
867   Duncan, B. N., Lamsal, L. N., Thompson, A. M., Yoshida, Y., Lu, Z., Streets, D. G.,
868   Hurwitz, M. M. and Pickering, K. E.: A space-based, high-resolution view of notable
869   changes in urban NOx pollution around the world (2005–2014), J. Geophys. Res.
870   Ocean., 121, 976–996, doi:10.1002/ 2015JD024121, 2016.
871   Emanuel, K. A.: A Scheme for Representing Cumulus Convection in Large-Scale
872   Models, J. Atmos. Sci., 48(21), 2313–2329, doi:10.1175/1520-
873   0469(1991)048<2313:ASFRCC>2.0.CO;2, 1991.
874   Erisman, J. A. N. W.: The Nanjing Declaration on Management of Reactive Nitrogen,
875   , 54(4), 286–287, 2004.
876   Erisman, J. W., Bleeker, A., Galloway, J. and Sutton, M. S.: Reduced nitrogen in
877   ecology and the environment, Environ. Pollut., 150(1), 140–149,
878   doi:10.1016/j.envpol.2007.06.033, 2007.
879   Escobar, H.: Amazon fires clearly linked to deforestation, scientists say, Science (80-
880   .)., 365(6456), 853, doi:10.1126/science.365.6456.853, 2019.
881   European Environment Agency: EMEP/EEA air pollutant emission inventory
882   guidebook 2019: Technical guidance to prepare national emission inventories., 2019.
883   Evangeliou, N., Hamburger, T., Talerko, N., Zibtsev, S., Bondar, Y., Stohl, A.,
884   Balkanski, Y., Mousseau, T. A. and Møller, A. P.: Reconstructing the Chernobyl
885   Nuclear Power Plant (CNPP) accident 30 years after. A unique database of air
886   concentration and deposition measurements over Europe, Environ. Pollut., (August),
887   doi:10.1016/j.envpol.2016.05.030, 2016.
888   Faulkner, W. B. and Shaw, B. W.: Review of ammonia emission factors for United
889   States animal agriculture, Atmos. Environ., 42(27), 6567–6574,
890   doi:10.1016/j.atmosenv.2008.04.021, 2008.
891   Flechard, C. R. and Fowler, D.: Atmospheric ammonia at a moorland site. I: The
892   meteorological control of ambient ammonia concentrations and the influence of local
893   sources, Q. J. R. Meteorol. Soc., 124(547), 733–757, doi:10.1256/smsqj.54704,
894   1998.

Folberth, G. A., Hauglustaine, D. A., Lathière, J. and Brocheton, F.: Interactive chemistry in the Laboratoire de Météorologie Dynamique general circulation model: model description and impact analysis of biogenic hydrocarbons on tropospheric chemistry, Atmos. Chem. Phys., 6(8), 2273–2319, doi:10.5194/acp-6-2273-2006, 2006.

Fowler, D., Muller, J. B. A., Smith, R. I., Dragosits, U., Skiba, U., Sutton, M. A. and Brimblecombe, P.: A CHRONOLOGY OF NITROGEN DEPOSITION IN THE UK, , 2, 9–23, 2004.

De Foy, B., Lu, Z. and Streets, D. G.: Satellite NO2 retrievals suggest China has exceeded its NOx reduction goals from the twelfth Five-Year Plan, Sci. Rep., 6(May 2016), 1–9, doi:10.1038/srep35912, 2016.

Gelaro, R., McCarty, W., Suárez, M. J., Todling, R., Molod, A., Takacs, L., Randles, C. A., Darmenov, A., Bosilovich, M. G., Reichle, R., Wargan, K., Coy, L., Cullather, R., Draper, C., Akella, S., Buchard, V., Conaty, A., da Silva, A. M., Gu, W., Kim, G. K., Koster, R., Lucchesi, R., Merkova, D., Nielsen, J. E., Partyka, G., Pawson, S., Putman, W., Rienecker, M., Schubert, S. D., Sienkiewicz, M. and Zhao, B.: The modern-era retrospective analysis for research and applications, version 2 (MERRA-2), J. Clim., 30(14), 5419–5454, doi:10.1175/JCLI-D-16-0758.1, 2017.

Giglio, L., Randerson, J. T. and van der Werf, G. R.: Analysis of daily, monthly, and annual burned area using the fourth-generation global fire emissions database (GFED4), J. Geophys. Res. Biogeosciences, 118, 317–328, doi:10.1002/jgrg.20042, 2013, 2013.

Gu, B., Sutton, M. A., Chang, S. X., Ge, Y. and Chang, J.: Agricultural ammonia emissions contribute to China's urban air pollution, Front. Ecol. Environ., 12(5), 265–266, doi:10.1890/14.WB.007, 2014.

Hand, J. L., Schichtel, B. A., Malm, W. C. and Pitchford, M. L.: Particulate sulfate ion concentration and SO2 emission trends in the United States from the early 1990s through 2010, Atmos. Chem. Phys., 12(21), 10353–10365, doi:10.5194/acp-12-10353-2012, 2012.

Hauglustaine, D. A., Hourdin, F., Jourdain, L., Filiberti, M.-A., Walters, S., Lamarque, J.-F. and Holland, E. A.: Interactive chemistry in the Laboratoire de Meteorologie Dynamique general circulation model: Description and background tropospheric chemistry evaluation, J. Geophys. Res., 109(D04314), doi:10.1029/2003JD003957, 2004.

Hauglustaine, D. A., Balkanski, Y. and Schulz, M.: A global model simulation of present and future nitrate aerosols and their direct radiative forcing of climate, Atmos. Chem. Phys., 14(20), 11031–11063, doi:10.5194/acp-14-11031-2014, 2014.

Henze, D. K., Shindell, D. T., Akhtar, F., Spurr, R. J. D., Pinder, R. W., Loughlin, D., Kopacz, M., Singh, K. and Shim, C.: Spatially Refined Aerosol Direct Radiative Forcing Efficiencies, Environ. Sci. Technol., 46, 9511–9518, doi:10.1021/es301993s, 2012.

Hertel, O., Skjoth, C. A., Reis, S., Bleeker, A., Harrison, R. M., Cape, J. N., Fowler, D., Skiba, U., Simpson, D., Jickells, T., Kulmala, M., Gyldenkærne, S., Sorensen, L. L., Erisman, J. W. and Sutton, M. A.: Governing processes for reactive nitrogen compounds in the European atmosphere, Biogeosciences, 9(12), 4921–4954, doi:10.5194/bg-9-4921-2012, 2012.

Hoesly, R. M., Smith, S. J., Feng, L., Klimont, Z., Janssens-Maenhout, G., Pitkanen, T., Seibert, J. J., Vu, L., Andres, R. J., Bolt, R. M., Bond, T. C., Dawidowski, L., Kholod, N., Kurokawa, J., Li, M., Liu, L., Lu, Z., Moura, M. C. P., O'Rourke, P. R. and Zhang, Q.: Historical (1750&ndash;2014)

945   anthropogenic emissions of reactive gases and aerosols from the Community
946   Emission Data System (CEDS), Geosci. Model Dev. Discuss., (March), 1–41,
947   doi:10.5194/gmd-2017-43, 2017.
948   Hourdin, F. and Armengaud, A.: The Use of Finite-Volume Methods for Atmospheric
949   Advection of Trace Species. Part I: Test of Various Formulations in a General
950   Circulation Model, Mon. Weather Rev., 127(5), 822–837, doi:10.1175/1520-
951   0493(1999)127<0822:TUOFVM>2.0.CO;2, 1999.
952   Hourdin, F., Musat, I., Bony, S., Braconnot, P., Codron, F., Dufresne, J. L., Fairhead,
953   L., Filiberti, M. A., Friedlingstein, P., Grandpeix, J. Y., Krinner, G., LeVan, P., Li, Z. X.
954   and Lott, F.: The LMDZ4 general circulation model: Climate performance and
955   sensitivity to parametrized physics with emphasis on tropical convection, Clim. Dyn.,
956   27(7–8), 787–813, doi:10.1007/s00382-006-0158-0, 2006.
957   Hov, Ø., Hjøllo, B. A. and Eliassen, A.: Transport distance of ammonia and
958   ammonium in Northern Europe: 2. Its relation to emissions of SO 2 and NO x, J.
959   Geophys. Res., 99(D9), 18749, doi:10.1029/94jd00910, 1994.
960   Kajino, M., Ueda, H., Satsumabayashi, H. and An, J.: Impacts of the eruption of
961   Miyakejima Volcano on air quality over far east Asia, J. Geophys. Res. D Atmos.,
962   109(21), 1–11, doi:10.1029/2004JD004762, 2004.
963   Kean, A. J., Littlejohn, D., Ban-Weiss, G. A., Harley, R. A., Kirchstetter, T. W. and
964   Lunden, M. M.: Trends in on-road vehicle emissions of ammonia, Atmos. Environ.,
965   43(8), 1565–1570, doi:10.1016/j.atmosenv.2008.09.085, 2009.
966   Kharol, S. K., Shephard, M. W., McLinden, C. A., Zhang, L., Sioris, C. E., O'Brien, J.
967   M., Vet, R., Cady-Pereira, K. E., Hare, E., Siemons, J. and Krotkov, N. A.: Dry
968   Deposition of Reactive Nitrogen From Satellite Observations of Ammonia and
969   Nitrogen Dioxide Over North America, Geophys. Res. Lett., 45(2), 1157–1166,
970   doi:10.1002/2017GL075832, 2018.
971   Klimont, Z., Smith, S. J. and Cofala, J.: The last decade of global anthropogenic
972   sulfur dioxide: 2000-2011 emissions, Environ. Res. Lett., 8(1), doi:10.1088/1748-
973   9326/8/1/014003, 2013.
974   Klimont, Z., Kupiainen, K., Heyes, C., Purohit, P., Cofala, J., Rafaj, P., Borken-
975   Kleefeld, J. and Schöpp, W.: Global anthropogenic emissions of particulate matter
976   including black carbon, Atmos. Chem. Phys., 17, 8681–8723, doi:10.5194/acp-17- 50
977   8681-2017, 2017.
978   Koukouli, M. E., Theys, N., Ding, J., Zyrichidou, I., Mijling, B., Balis, D. and Johannes
979   Van Der A, R.: Updated SO2 emission estimates over China using OMI/Aura
980   observations, Atmos. Meas. Tech., 11(3), 1817–1832, doi:10.5194/amt-11-1817-
981   2018, 2018.
982   Krinner, G., Viovy, N., de Noblet-Ducoudré, N., Ogée, J., Polcher, J., Friedlingstein,
983   P., Ciais, P., Sitch, S. and Prentice, I. C.: A dynamic global vegetation model for
984   studies of the coupled atmosphere-biosphere system, Global Biogeochem. Cycles,
985   19(1), n/a--n/a, doi:10.1029/2003GB002199, 2005.
986   Krotkov, N. A., McLinden, C. A., Li, C., Lamsal, L. N., Celarier, E. A., Marchenko, S.
987   V., Swartz, W. H., Bucsela, E. J., Joiner, J., Duncan, B. N., Folkert Boersma, K.,
988   Pepijn Veefkind, J., Levelt, P. F., Fioletov, V. E., Dickerson, R. R., He, H., Lu, Z. and
989   Streets, D. G.: Aura OMI observations of regional SO2 and NO2 pollution changes
990   from 2005 to 2015, Atmos. Chem. Phys., 16(7), 4605–4629, doi:10.5194/acp-16-
991   4605-2016, 2016.
992   Kuttippurath, J., Singh, A., Dash, S. P., Mallick, N., Clerbaux, C., Van Damme, M.,
993   Clarisse, L., Coheur, P. F., Raj, S., Abbhishek, K. and Varikoden, H.: Record high
994   levels of atmospheric ammonia over India: Spatial and temporal analyses, Sci. Total

995   Environ., 740, 139986, doi:10.1016/j.scitotenv.2020.139986, 2020.

996   Lachatre, M., Fortems-Cheiney, A., Foret, G., Siour, G., Dufour, G., Clarisse, L.,
997   Clerbaux, C., Coheur, P. F., Van Damme, M. and Beekmann, M.: The unintended
998   consequence of SO2 and NO2 regulations over China: Increase of ammonia levels
999   and impact on PM2.5 concentrations, Atmos. Chem. Phys., 19(10), 6701–6716,
1000   doi:10.5194/acp-19-6701-2019, 2019.

1001   Lehmann, C. M. B., Bowersox, V. C., Larson, R. S. and Larson, S. M.: Monitoring
1002   long-term trends in sulfate and ammonium in US precipitation: Results from the
1003   national atmospheric deposition program/national trends network, Water, Air, Soil
1004   Pollut. Focus, 7(1–3), 59–66, doi:10.1007/s11267-006-9100-z, 2007.

1005   Leip, A., Billen, G., Garnier, J., Grizzetti, B., Lassaletta, L., Reis, S., Simpson, D.,
1006   Sutton, M. a, de Vries, W., Weiss, F. and Westhoek, H.: Impacts of European
1007   livestock production: nitrogen, sulphur, phosphorus and greenhouse gas emissions,
1008   land-use, water eutrophication and biodiversity, Environ. Res. Lett., 10(11), 115004,
1009   doi:10.1088/1748-9326/10/11/115004, 2015.

1010   Lelieveld, J., Evans, J. S., Fnais, M., Giannadaki, D. and Pozzer, A.: The contribution
1011   of outdoor air pollution sources to premature mortality on a global scale., Nature,
1012   525(7569), 367–71, doi:10.1038/nature15371, 2015.

1013   Li, C., Martin, R. V, Shephard, M. W., Pereira, K. C., Cooper, M. J., Kaiser, J., Lee,
1014   C. J., Zhang, L. and Henze, D. K.: Assessing the Iterative Finite Difference Mass
1015   Balance and 4D - Var Methods to Derive Ammonia Emissions Over North America
1016   Using Synthetic Observations, , 4222–4236, doi:10.1029/2018JD030183, 2019.

1017   Li, M., Liu, H., Geng, G., Hong, C., Liu, F., Song, Y., Tong, D., Zheng, B., Cui, H.,
1018   Man, H., Zhang, Q. and He, K.: Anthropogenic emission inventories in China: A
1019   review, Natl. Sci. Rev., 4(6), 834–866, doi:10.1093/nsr/nwx150, 2017.

1020   Li, M., Klimont, Z., Zhang, Q., Martin, R. V., Zheng, B., Heyes, C., Cofala, J., Zhang,
1021   Y. and He, K.: Comparison and evaluation of anthropogenic emissions of SO2 and
1022   NOx over China, Atmos. Chem. Phys., 18(5), 3433–3456, doi:10.5194/acp-18-3433-
1023   2018, 2018.

1024   Lin, J. T., McElroy, M. B. and Boersma, K. F.: Constraint of anthropogenic NOx
1025   emissions in China from different sectors: A new methodology using multiple satellite
1026   retrievals, Atmos. Chem. Phys., 10(1), 63–78, doi:10.5194/acp-10-63-2010, 2010.

1027   Liu, F., Beirle, S., Zhang, Q., van der A, R. J., Zheng, B., Tong, D. and He, K.: NOx
1028   emission trends over Chinese cities estimated from OMI observations during 2005 to
1029   2015, Atmos. Chem. Phys. Discuss., (2), 1–21, doi:10.5194/acp-2017-369, 2017.

1030   Liu, M., Huang, X., Song, Y., Xu, T., Wang, S., Wu, Z., Hu, M., Zhang, L., Zhang, Q.,
1031   Pan, Y. and Zhu, T.: Rapid SO2 emission reductions significantly increase
1032   tropospheric ammonia concentrations over the North China Plain, Atmos. Chem.
1033   Phys., (18), 17933–17943, doi:10.5194/acp-18-17933-2018, 2018.

1034   Makar, P. A., Moran, M. D., Zheng, Q., Cousineau, S., Sassi, M., Duhamel, A.,
1035   Besner, M., Davignon, D., Crevier, L. P. and Bouchet, V. S.: Modelling the impacts of
1036   ammonia emissions reductions on North American air quality, Atmos. Chem. Phys.,
1037   9(18), 7183–7212, doi:10.5194/acp-9-7183-2009, 2009.

1038   Malm, W. C.: Spatial and monthly trends in speciated fine particle concentration in
1039   the United States, J. Geophys. Res., 109(D3), D03306, doi:10.1029/2003JD003739,
1040   2004.

1041   Malm, W. C., Schichtel, B. A., Barna, M. G., Gebhart, K. A., Rodriguez, M. A., Collett,
1042   J. L., Carrico, C. M., Benedict, K. B., Prenni, A. J. and Kreidenweis, S. M.: Aerosol
1043   species concentrations and source apportionment of ammonia at Rocky Mountain
1044   National Park, J. Air Waste Manag. Assoc., 63(11), 1245–1263,

doi:10.1080/10962247.2013.804466, 2013.

van Marle, M. J. E., Field, R. D., van der Werf, G. R., Estrada de Wagt, I. A., Houghton, R. A., Rizzo, L. V., Artaxo, P. and Tsigaridis, K.: Fire and deforestation dynamics in Amazonia (1973–2014), Global Biogeochem. Cycles, 31(1), 24–38, doi:10.1002/2016GB005445, 2017.

McQuilling, A. M.: Ammonia emissions from livestock in the United States: From farm emissions models to a new national inventory, ProQuest Diss. Theses, 168 [online] Available from: https://search.proquest.com/docview/1841254436?accountid=133571%0Ahttp://www .yidu.edu.cn/educhina/educhina.do?artifact=&svalue=Ammonia+emissions+from+live stock+in+the+United+States%3A+From+farm+emissions+models+to+a+new+nation al+inventory&stype=2&s=on%0Ah, 2016.

Min Hao, W., Petkov, A., Nordgren, B. L., Corley, R. E., Silverstein, R. P., Urbanski, S. P., Evangeliou, N., Balkanski, Y. and Kinder, B. L.: Daily black carbon emissions from fires in northern Eurasia for 2002-2015, Geosci. Model Dev., 9(12), doi:10.5194/gmd-9-4461-2016, 2016.

Möller, D. and Schieferdecker, H.: A relationship between agricultural NH 3 emissions and the atmospheric SO 2 content over industrial areas, Atmos. Environ., 19(5), 695–700, doi:10.1016/0004-6981(85)90056-3, 1985.

Norman, M. and Leck, C.: Distribution of marine boundary layer ammonia over the Atlantic and Indian Oceans during the Aerosols99 cruise, J. Geophys. Res. D Atmos., 110(16), 1–11, doi:10.1029/2005JD005866, 2005.

Pan, Y., Tian, S., Zhao, Y., Zhang, L., Zhu, X., Gao, J., Huang, W., Zhou, Y., Song, Y., Zhang, Q. and Wang, Y.: Identifying Ammonia Hotspots in China Using a National Observation Network, Environ. Sci. Technol., 52(7), 3926–3934, doi:10.1021/acs.est.7b05235, 2018.

Parzen, E.: On the Estimation of Probability Density Functions and Mode, Ann. Math. Stat., 33, 1065–1076, 1962.

Paulot, F., Jacob, D. J., Pinder, R. W., Bash, J. O., Travis, K. and Henze, D. K.: Ammonia emissions in the United States, European Union, and China derived by high-resolution inversion of ammonium wet deposition data: Interpretation with a new agricultural emissions inventory (MASAGE-NH3), J. Geophys. Res. Atmos., 119(7), 4343–4364, doi:10.1002/2013JD021130, 2014.

Pinder, R. W., Gilliland, A. B. and Dennis, R. L.: Environmental impact of atmospheric NH$_3$ emissions under present and future conditions in the eastern United States, Geophys. Res. Lett., 35(12), 1–6, doi:10.1029/2008GL033732, 2008.

Pope III, C. A., Burnett, R. T., Thun, M. J., Calle, E. E., Krewski, D. and Thurston, G. D.: Lung Cancer, Cardiopulmonary Mortality, and Long-term Exposure to Fine Particulate Air Pollution, J. Am. Med. Assoc., 287(9), 1132–1141, doi:10.1001/jama.287.9.1132, 2002.

Quinn, P. K., Bates, T. S. and Johnson, J. E.: Interactions Between the Sulfur and Reduced Nitrogen Cycles Over the Central Pacific Ocean, J. Geophys. Res., 95(D10), 16405–16416, 1990.

R'Honi, Y., Clarisse, L., Clerbaux, C., Hurtmans, D., Duflot, V., Turquety, S., Ngadi, Y. and Coheur, P. F.: Exceptional emissions of NH3 and HCOOH in the 2010 Russian wildfires, Atmos. Chem. Phys., 13(1), 4171–4181, doi:10.5194/acp-13-4171-2013, 2013.

Reche, C., Viana, M., Pandolfi, M., Alastuey, A., Moreno, T., Amato, F., Ripoll, A. and Querol, X.: Urban NH 3 levels and sources in a Mediterranean environment, Atmos.

Environ., 57, 153–164, doi:10.1016/j.atmosenv.2012.04.021, 2012.

Reis, S., Pinder, R. W., Zhang, M., Lijie, G. and Sutton, M. A.: Reactive nitrogen in atmospheric emission inventories, Atmos. Chem. Phys., 9(19), 7657–7677, doi:10.5194/acp-9-7657-2009, 2009.

Reis, S., Grennfelt, P., Klimont, Z., Amann, M., ApSimon, H., Hettelingh, J. P., Holland, M., LeGall, A. C., Maas, R., Posch, M., Spranger, T., Sutton, M. A. and Williams, M.: From acid rain to climate change, Science (80-.)., 338(6111), 1153–1154, doi:10.1126/science.1226514, 2012.

Renka, R. J.: Multivariate Interpolation of Large Sets of Scattered Data, ACM Trans. Math. Softw., 14(2), 139–148, doi:10.1145/45054.45055, 1988.

Saikawa, E., Kim, H., Zhong, M., Avramov, A., Zhao, Y., Janssens-Maenhout, G., Kurokawa, J. I., Klimont, Z., Wagner, F., Naik, V., Horowitz, L. W. and Zhang, Q.: Comparison of emissions inventories of anthropogenic air pollutants and greenhouse gases in China, Atmos. Chem. Phys., 17(10), 6393–6421, doi:10.5194/acp-17-6393-2017, 2017a.

Saikawa, E., Trail, M., Zhong, M., Wu, Q., Young, C. L., Janssens-Maenhout, G., Klimont, Z., Wagner, F., Kurokawa, J. I., Nagpure, A. S. and Gurjar, B. R.: Uncertainties in emissions estimates of greenhouse gases and air pollutants in India and their impacts on regional air quality, Environ. Res. Lett., 12(6), doi:10.1088/1748-9326/aa6cb4, 2017b.

Schulz, M.: Constraining model estimates of the aerosol Radiative Forcing, Université Pierre et Marie Curie, Paris VI., 2007.

Scott, D. W.: Multivariate density estimation: Theory, practice, and visualization: Second edition., 2015.

Seinfeld, J. H. and Pandis, S. N.: Atmospheric Chemistry and Physics. From Air Pollution to Climate Change, 2nd ed., John Wiley & Sons, NY., 2000.

Shephard, M. W. and Cady-Pereira, K. E.: Cross-track Infrared Sounder (CrIS) satellite observations of tropospheric ammonia, Atmos. Meas. Tech., 8(3), 1323–1336, doi:10.5194/amt-8-1323-2015, 2015.

Shephard, M. W., McLinden, C. A., Cady-Pereira, K. E., Luo, M., Moussa, S. G., Leithead, A., Liggio, J., Staebler, R. M., Akingunola, A., Makar, P., Lehr, P., Zhang, J., Henze, D. K., Millet, D. B., Bash, J. O., Zhu, L., Wells, K. C., Capps, S. L., Chaliyakunnel, S., Gordon, M., Hayden, K., Brook, J. R., Wolde, M. and Li, S. M.: Tropospheric Emission Spectrometer (TES) satellite observations of ammonia, methanol, formic acid, and carbon monoxide over the Canadian oil sands: Validation and model evaluation, Atmos. Meas. Tech., 8(12), 5189–5211, doi:10.5194/amt-8-5189-2015, 2015.

Shephard, M. W., Dammers, E., E. Cady-Pereira, K., K. Kharol, S., Thompson, J., Gainariu-Matz, Y., Zhang, J., A. McLinden, C., Kovachik, A., Moran, M., Bittman, S., E. Sioris, C., Griffin, D., J. Alvarado, M., Lonsdale, C., Savic-Jovcic, V. and Zheng, Q.: Ammonia measurements from space with the Cross-track Infrared Sounder: Characteristics and applications, Atmos. Chem. Phys., 20(4), 2277–2302, doi:10.5194/acp-20-2277-2020, 2020.

Sickles, J. E. and Shadwick, D. S.: Air quality and atmospheric deposition in the eastern US: 20 years of change, Atmos. Chem. Phys., 15(1), 173–197, doi:10.5194/acp-15-173-2015, 2015.

Someya, Y., Imasu, R., Shiomi, K. and Saitoh, N.: Atmospheric ammonia retrieval from the TANSO-FTS / GOSAT thermal infrared sounder, , 1990, 309–321, 2020.

Sørensen, L. L., Hertel, O., Skjøth, C. A., Lund, M. and Pedersen, B.: Fluxes of ammonia in the coastal marine boundary layer, Atmos. Environ., 37(SUPPL. 1), 167–

177, doi:10.1016/S1352-2310(03)00247-4, 2003.

Stevens, C. J., Dupr, C., Dorland, E., Gaudnik, C., Gowing, D. J. G., Bleeker, A., Diekmann, M., Alard, D., Bobbink, R., Fowler, D., Corcket, E., Mountford, J. O., Vandvik, V., Aarrestad, P. A., Muller, S. and Dise, N. B.: Nitrogen deposition threatens species richness of grasslands across Europe, Environ. Pollut., 158(9), 2940–2945, doi:10.1016/j.envpol.2010.06.006, 2010.

Streets, D. G., Canty, T., Carmichael, G. R., de Foy, B., Dickerson, R. R., Duncan, B. N., Edwards, D. P., Haynes, J. A., Henze, D. K., Houyoux, M. R., Jacob, D. J., Krotkov, N. A., Lamsal, L. N., Liu, Y., Lu, Z., Martin, R. V, Pfister, G. G., Pinder, R. W., Salawitch, R. J. and Wecht, K. J.: Emissions estimation from satellite retrievals: A review of current capability, Atmos. Environ., 77, 1011–1042, doi:https://doi.org/10.1016/j.atmosenv.2013.05.051, 2013.

Sutton, M. A., Fowler, D., Moncrieft, J. B. and Storeton-West, R. L.: The exchange of atmospheric ammonia with vegetated surfaces. II: Fertilized vegetation, Q. J. R. Meteorol. Soc., 119(513), 1047–1070, doi:10.1002/qj.49711951310, 1993.

Sutton, M. A., Dragosits, U., Tang, Y. S. and Fowler, D.: Ammonia emissions from non-agricultural sources in the UK, , 34(August 1999), 2000.

Sutton, M. A., Erisman, J. W., Dentener, F. and Möller, D.: Ammonia in the environment: From ancient times to the present, Environ. Pollut., 156(3), 583–604, doi:10.1016/j.envpol.2008.03.013, 2008.

Tanvir, A., Khokhar, M. F., Javed, Z., Sandhu, O., Mustansar, T. and Shoaib, A.: Spatiotemporal evolution of atmospheric ammonia columns over the indo-gangetic plain by exploiting satellite observations, Adv. Meteorol., 2019, doi:10.1155/2019/7525479, 2019.

Torseth, K., Aas, W., Breivik, K., Fjeraa, A. M., Fiebig, M., Hjellbrekke, A. G., Lund Myhre, C., Solberg, S. and Yttri, K. E.: Introduction to the European Monitoring and Evaluation Programme (EMEP) and observed atmospheric composition change during 1972-2009, Atmos. Chem. Phys., 12(12), 5447–5481, doi:10.5194/acp-12-5447-2012, 2012.

Turner, A. J., Henze, D. K., Martin, R. V. and Hakami, A.: The spatial extent of source influences on modeled column concentrations of short-lived species, Geophys. Res. Lett., 39(12), 1–5, doi:10.1029/2012GL051832, 2012.

Uematsu, M., Toratani, M., Kajino, M., Narita, Y., Senga, Y. and Kimoto, T.: Enhancement of primary productivity in the western North Pacific caused by the eruption of the Miyake-jima Volcano, Geophys. Res. Lett., 31(6), n/a-n/a, doi:10.1029/2003gl018790, 2004.

Vestreng, V., Myhre, G., Fagerli, H., Reis, S. and Tarrasón, L.: Twenty-five years of continuous sulphur dioxide emission reduction in Europe, Atmos. Chem. Phys., 7(13), 3663–3681, doi:10.5194/acp-7-3663-2007, 2007.

Vincenty, T.: Direct and inverse solutions of geodesics on the ellipsoid with application of nested equations, Surv. Rev. XXIII (misprinted as XXII), 176, 88–93, 1975.

De Vries, W., Kros, J., Reinds, G. J. and Butterbach-Bahl, K.: Quantifying impacts of nitrogen use in European agriculture on global warming potential, Curr. Opin. Environ. Sustain., 3(5), 291–302, doi:10.1016/j.cosust.2011.08.009, 2011.

Wang, J., Zhao, B., Wang, S., Yang, F., Xing, J., Morawska, L., Ding, A., Kulmala, M., Kerminen, V. M., Kujansuu, J., Wang, Z., Ding, D., Zhang, X., Wang, H., Tian, M., Petäjä, T., Jiang, J. and Hao, J.: Particulate matter pollution over China and the effects of control policies, Sci. Total Environ., 584–585, 426–447, doi:10.1016/j.scitotenv.2017.01.027, 2017.

Wang, Y., Zhang, Q. Q., He, K., Zhang, Q. and Chai, L.: Sulfate-nitrate-ammonium aerosols over China: Response to 2000-2015 emission changes of sulfur dioxide, nitrogen oxides, and ammonia, Atmos. Chem. Phys., 13(5), 2635–2652, doi:10.5194/acp-13-2635-2013, 2013.

Warner, J. X., Dickerson, R. R., Wei, Z., Strow, L. L., Wang, Y. and Liang, Q.: Increased atmospheric ammonia over the world's major agricultural areas detected from space, Geophys. Res. Lett., 1–10, doi:10.1002/2016GL072305, 2017.

Webb, J., Menzi, H., Pain, B. F., Misselbrook, T. H., Dämmgen, U., Hendriks, H. and Döhler, H.: Managing ammonia emissions from livestock production in Europe, Environ. Pollut., 135(3 SPEC. ISS.), 399–406, doi:10.1016/j.envpol.2004.11.013, 2005.

Whitburn, S., Van Damme, M., Kaiser, J. W., Van Der Werf, G. R., Turquety, S., Hurtmans, D., Clarisse, L., Clerbaux, C. and Coheur, P. F.: Ammonia emissions in tropical biomass burning regions: Comparison between satellite-derived emissions and bottom-up fire inventories, Atmos. Environ., 121, 42–54, doi:10.1016/j.atmosenv.2015.03.015, 2014.

Whitburn, S., Van Damme, M., Clarisse, L., Bauduin, S., Heald, C. L., Hadji-Lazaro, J., Hurtmans, D., Zondlo, M. A., Clerbaux, C. and Coheur, P. F.: A flexible and robust neural network IASI-NH3 retrieval algorithm, J. Geophys. Res., 121(11), 6581–6599, doi:10.1002/2016JD024828, 2016a.

Whitburn, S., Damme, M. Van, Clarisse, L., Turquety, S., Clerbaux, C. and Coheur, P. -.: Peat fires doubled annual ammonia emissions in Indonesia during the 2015 El Niño, Geophys. Res. Lett., doi:10.1002/2016GL070620, 2016b.

Xing, J., Mathur, R., Pleim, J., Hogrefe, C., Gan, C. M., Wong, D. C., Wei, C., Gilliam, R. and Pouliot, G.: Observations and modeling of air quality trends over 1990-2010 across the Northern Hemisphere: China, the United States and Europe, Atmos. Chem. Phys., 15(5), 2723–2747, doi:10.5194/acp-15-2723-2015, 2015.

Xu, L. and Penner, J. E.: Global simulations of nitrate and ammonium aerosols and their radiative effects, Atmos. Chem. Phys., 12(20), 9479–9504, doi:10.5194/acp-12-9479-2012, 2012.

Xu, P., Liao, Y. J., Lin, Y. H., Zhao, C. X., Yan, C. H., Cao, M. N., Wang, G. S. and Luan, S. J.: High-resolution inventory of ammonia emissions from agricultural fertilizer in China from 1978 to 2008, Atmos. Chem. Phys., 16(3), 1207–1218, doi:10.5194/acp-16-1207-2016, 2016.

Xu, R. T., Pan, S. F., Chen, J., Chen, G. S., Yang, J., Dangal, S. R. S., Shepard, J. P. and Tian, H. Q.: Half-Century Ammonia Emissions From Agricultural Systems in Southern Asia: Magnitude, Spatiotemporal Patterns, and Implications for Human Health, GeoHealth, 2(1), 40–53, doi:10.1002/2017gh000098, 2018.

Yang, K., Krotkov, N. A., Krueger, A. J., Carn, S. A., Bhartia, P. K. and Levelt, P. F.: Retrieval of large volcanic SO_2 columns from the Aura Ozone Monitoring Instrument: Comparison and limitations, J. Geophys. Res. Atmos., 112(24), 1–14, doi:10.1029/2007JD008825, 2007.

Zavyalov, V., Esplin, M., Scott, D., Esplin, B., Bingham, G., Hoffman, E., Lietzke, C., Predina, J., Frain, R., Suwinski, L., Han, Y., Major, C., Graham, B. and Phillips, L.: Noise performance of the CrIS instrument, , 118, 108–120, doi:10.1002/2013JD020457, 2013.

Zhang, L., Wright, L. P. and Asman, W. A. H.: Bi-directional air-surface exchange of atmospheric ammonia: A review of measurements and a development of a big-leaf model for applications in regional-scale air-quality models, J. Geophys. Res. Atmos., 115(20), doi:10.1029/2009JD013589, 2010.

1245   Zhang, Q., He, K. and Hong, H.: Cleaning China ' s air, Nature, 484, 161–162, 2012.
1246   Zhao, C. and Wang, Y.: Assimilated inversion of NOx emissions over east Asia using
1247   OMINO2 column measurements, Geophys. Res. Lett., 36(6), 1–5,
1248   doi:10.1029/2008GL037123, 2009.
1249   Zheng, B., Tong, D., Li, M., Liu, F., Hong, C., Geng, G., Li, H., Li, X., Peng, L., Qi, J.,
1250   Yan, L., Zhang, Y., Zhao, H., Zheng, Y., He, K. and Zhang, Q.: Trends in China's
1251   anthropogenic emissions since 2010 as the consequence of clean air actions, Atmos.
1252   Chem. Phys., 18(19), 14095–14111, doi:10.5194/acp-18-14095-2018, 2018.
1253   Zhu, L., Henze, D. K., Cady-Pereira, K. E., Shephard, M. W., Luo, M., Pinder, R. W.,
1254   Bash, J. O. and Jeong, G. R.: Constraining U.S. ammonia emissions using TES
1255   remote sensing observations and the GEOS-Chem adjoint model, J. Geophys. Res.
1256   Atmos., 118(8), 3355–3368, doi:10.1002/jgrd.50166, 2013.
1257   Zhu, L., Henze, D. K., Bash, J. O., Cady-Pereira, K. E., Shephard, M. W., Luo, M.
1258   and Capps, S. L.: Sources and Impacts of Atmospheric NH3: Current Understanding
1259   and Frontiers for Modeling, Measurements, and Remote Sensing in North America,
1260   Curr. Pollut. Reports, 1(2), 95–116, doi:10.1007/s40726-015-0010-4, 2015.
1261
1262

 FIGURE LEGENDS
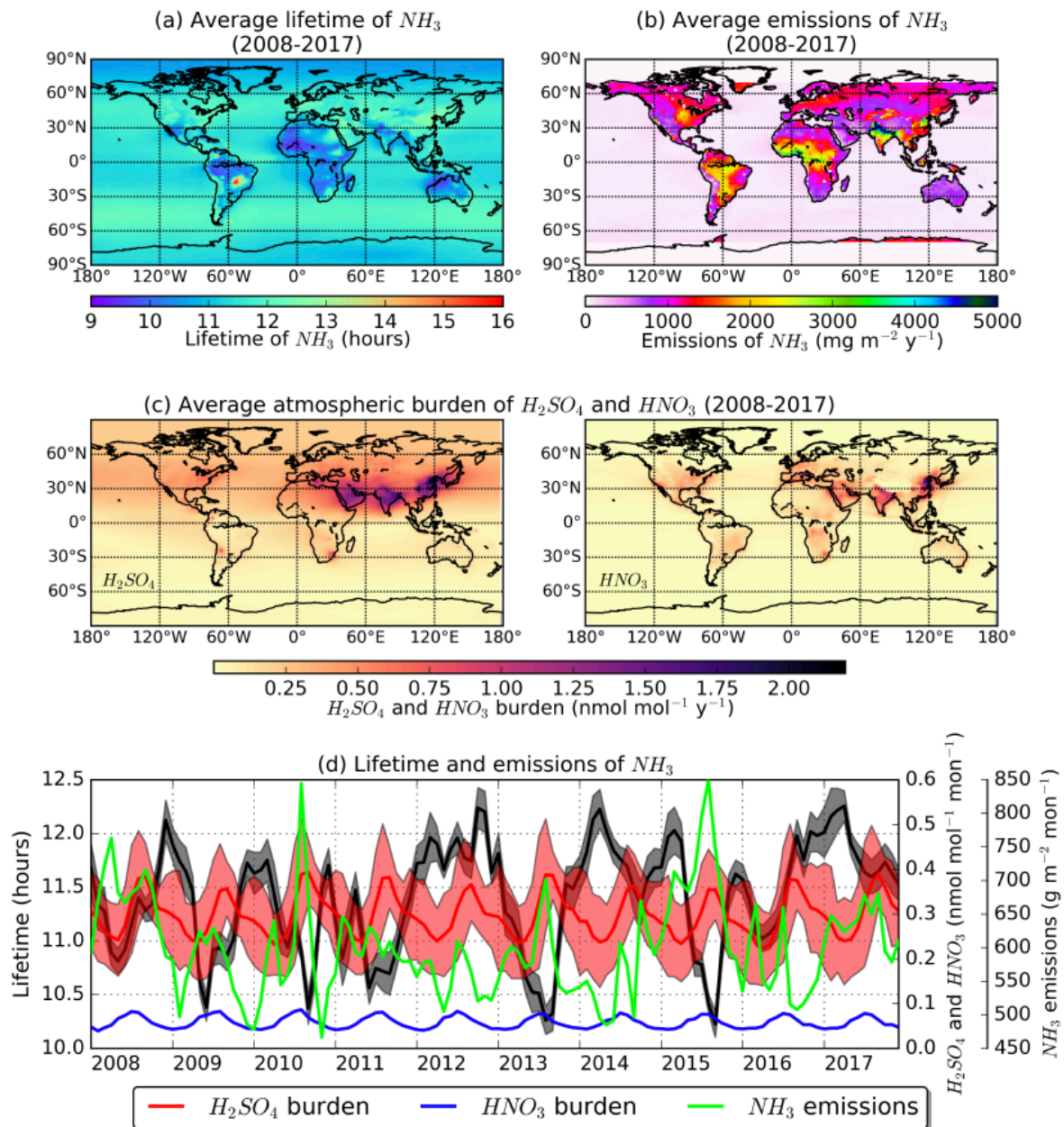
1265
1266 Figure 1. (a) 10-year average model lifetime of ammonia calculated from the LMDz-OR-INCA,
1267 (b) total annual emissions averaged over the 10-year period (NE emissions), (c) atmospheric
1268 burden of the reactants sulfuric and nitric acid calculated in the model, and (d) monthly
1269 timeseries of lifetime (black), ammonia emissions (green), sulfuric (red) and nitric acid column
1270 concentrations (blue) for the whole 10-year period.

1271
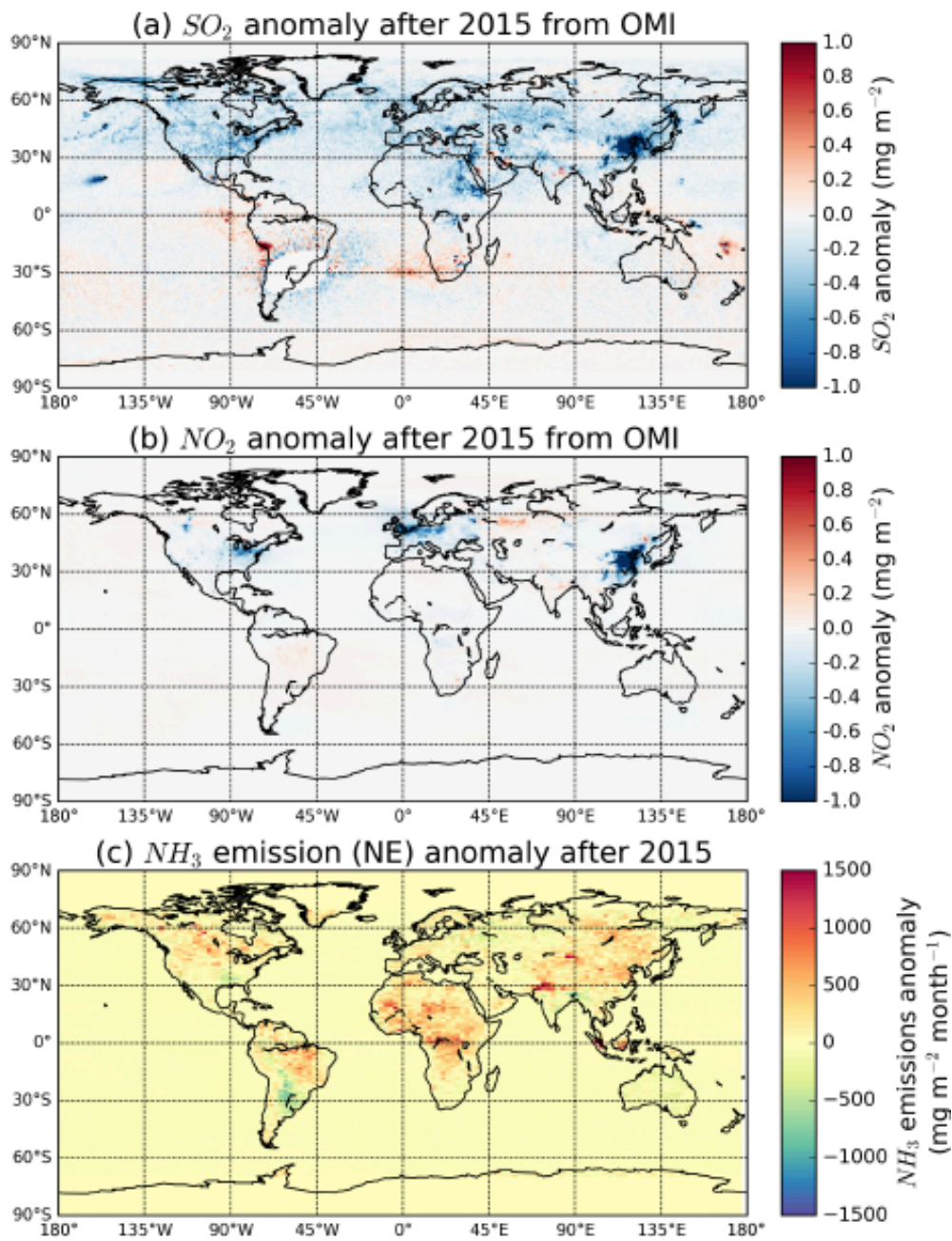
1272

1273   Figure 2. Annual average total column (a) sulfur dioxide and (b) nitrogen dioxide anomaly
1274   after 2015 from OMI, and (c) annual average emission anomaly of ammonia calculated from
1275   IASI in the present study (NE).

1276
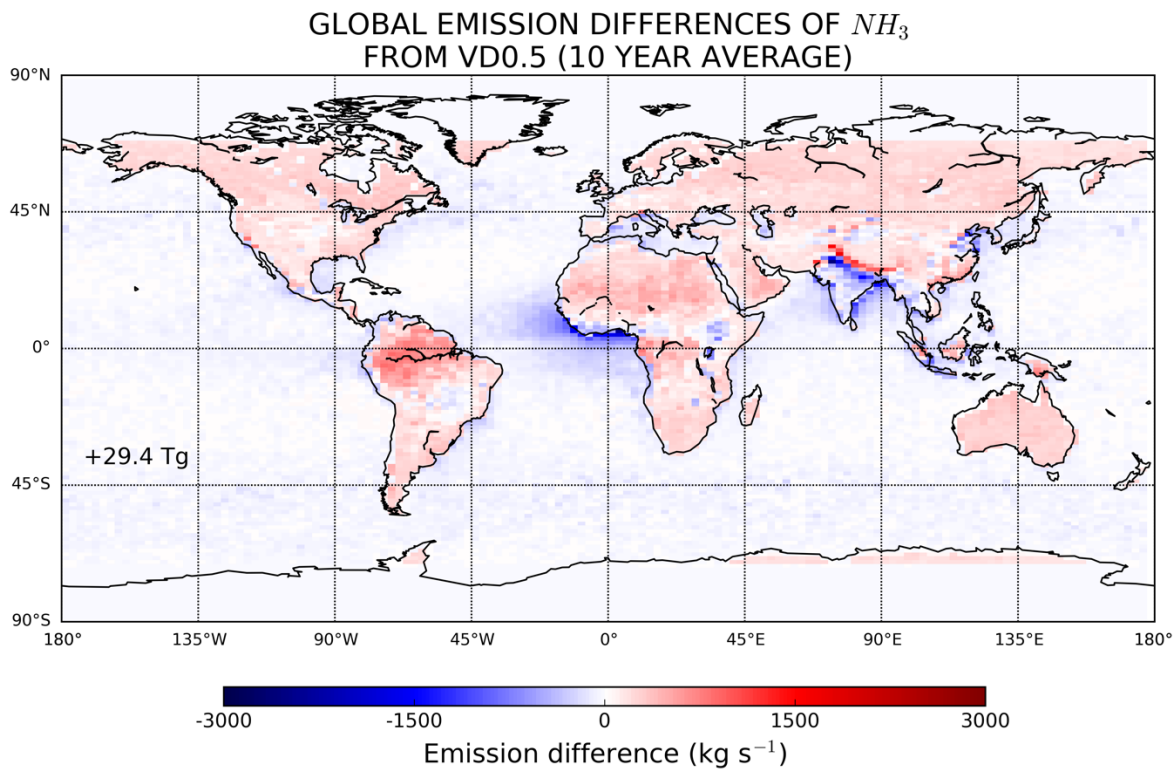
1277
1278 Figure 3. Global differences of ammonia emissions calculated in the present study (NE) from
1279 those calculated using Van Damme et al. (2018) gridded concentrations applying a constant
1280 lifetime of 0.5 days (VD0.5). The results are given as 10-year average (2008–2017) and the
1281 number denotes the annual difference in the emissions.

1282
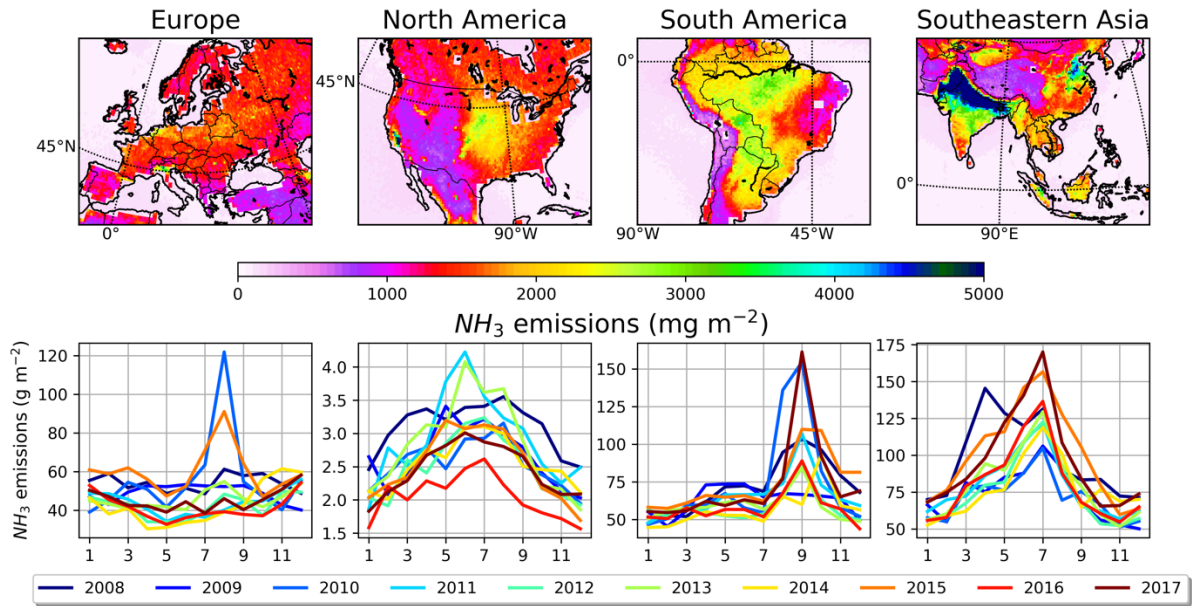
1283
1284 Figure 4. Total annual emissions of ammonia averaged over the 10-year period (2008–2017) in
1285 Europe, North and South America and Southeastern Asia, which are regions characterized by
1286 the largest contribution to global ammonia budget. In the bottom panels the monthly variation
1287 of the emissions is shown for each year of the study period.

1288
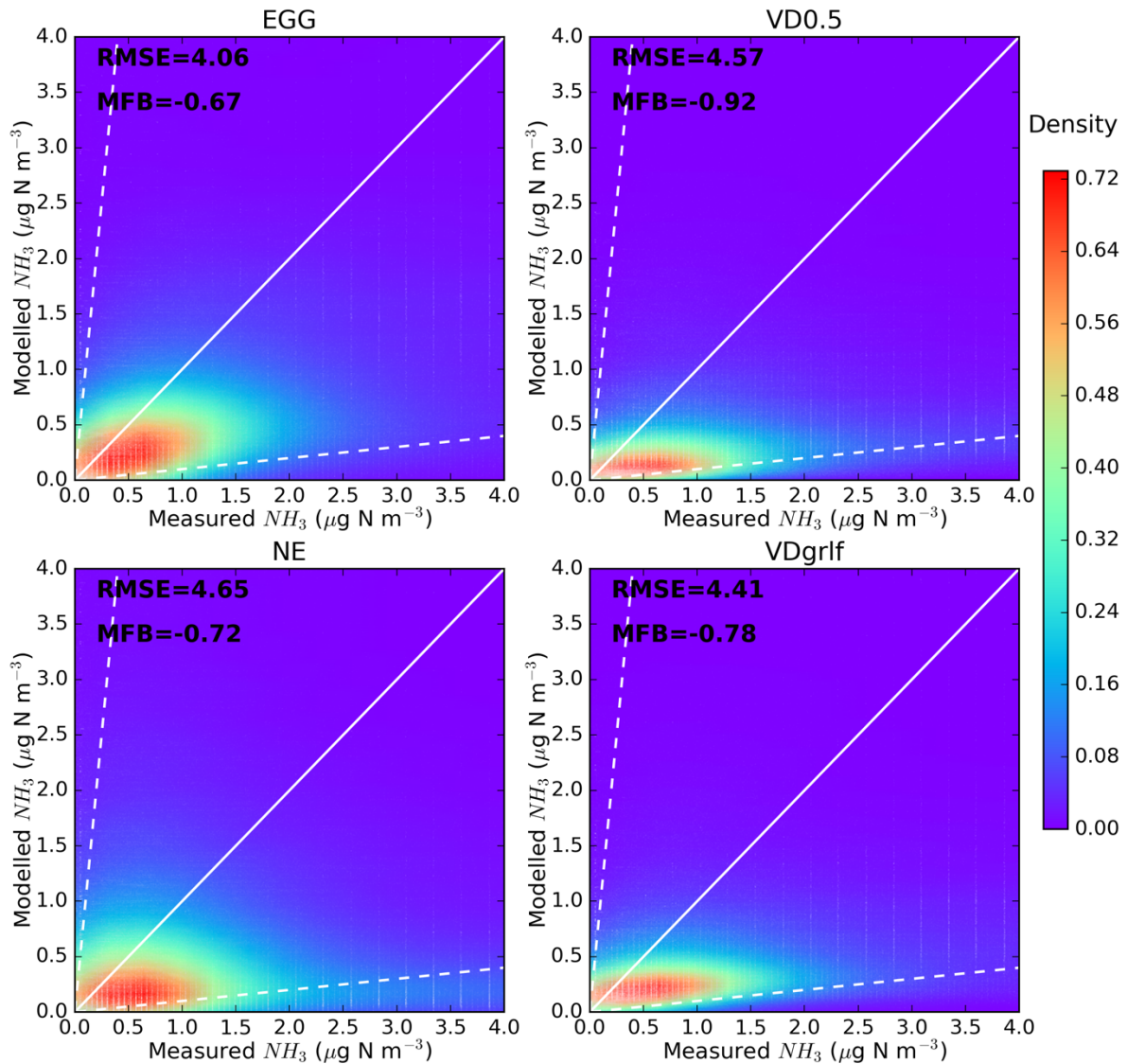
Figure 5. Validation of modelled concentrations of ammonia for different emissions datasets (EGG, VD0.5, NE and VDgrlf) against ground-based measurements from EMEP for the 10-year (2008–2017) study period. Scatterplots of modelled against measured concentrations for the aforementioned emission inventories were plotted with the Kernel density estimation, which is a way to estimate the probability density function (PDF) of a random variable in a non-parametric way.
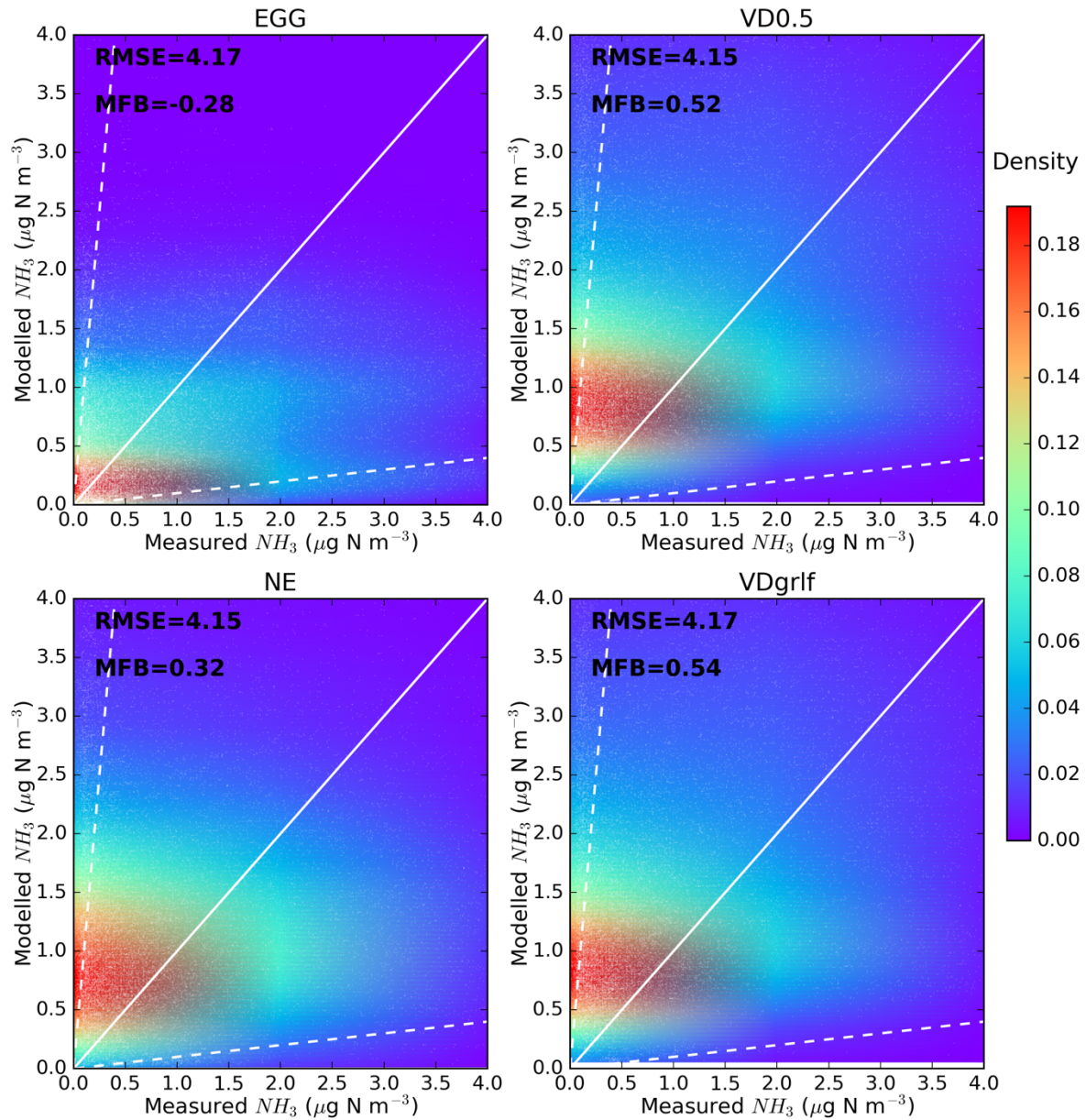
1297

1298   Figure 6. Validation of modelled concentrations of ammonia for different emissions datasets
1299   (EGG, VD0.5, NE and VDgrlf) against ground-based measurements from AMON for the 10-
1300   year (2008–2017) study period. Scatterplots of modelled against measured concentrations for
1301   the aforementioned emission inventories were plotted with the Kernel density estimation, which
1302   is a way to estimate the probability density function (PDF) of a random variable in a non-
1303   parametric way.

1304
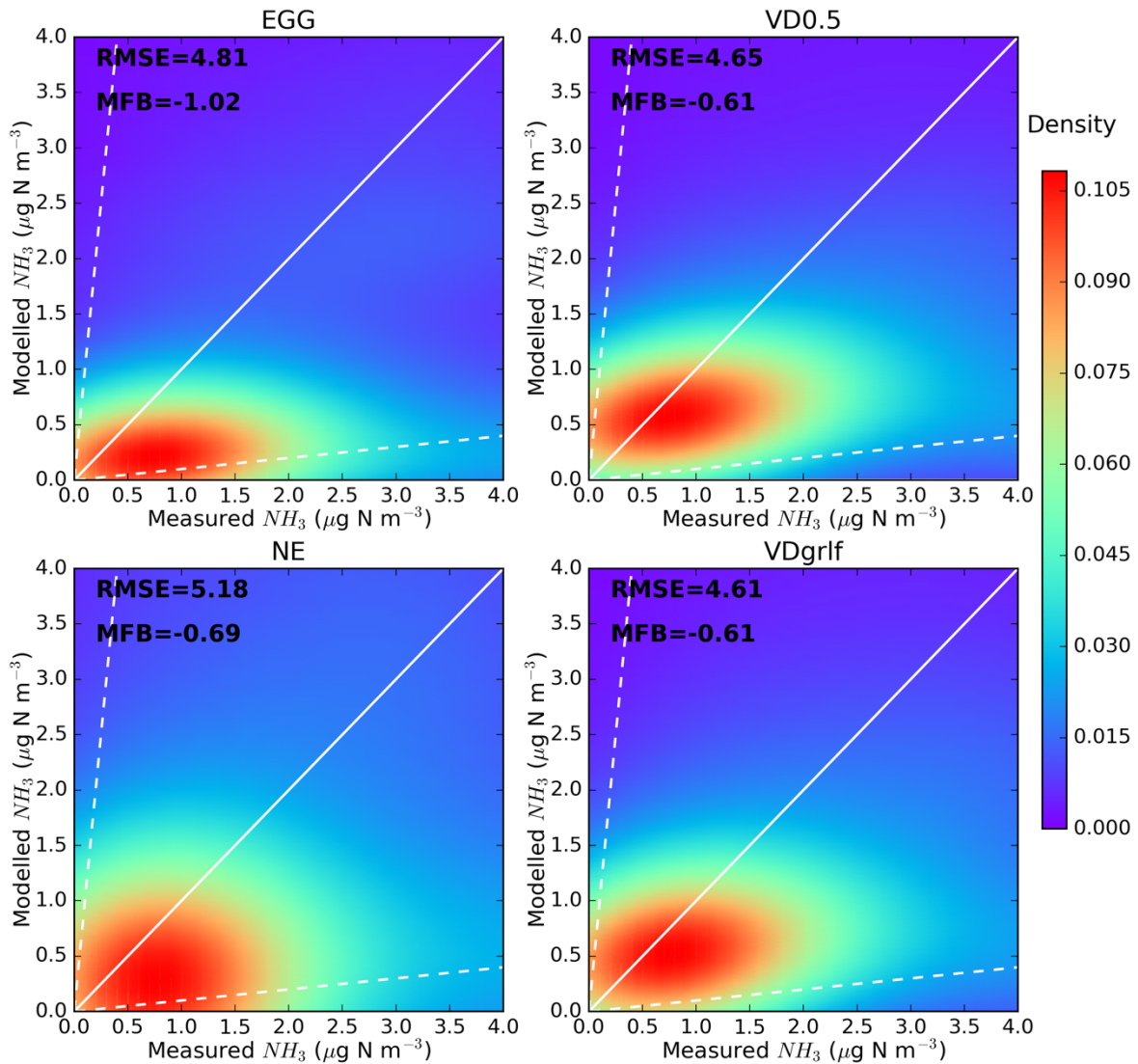
Figure 7. Validation of modelled concentrations of ammonia for different emissions datasets (EGG, VD0.5, NE and VDgrlf) against ground-based measurements from EANET for the 10-year (2008–2017) study period. Scatterplots of modelled against measured concentrations for the aforementioned emission inventories were plotted with the Kernel density estimation, which is a way to estimate the probability density function (PDF) of a random variable in a non-parametric way.

(a) ECLIPSEv5-GFED4-GEIA (EGG)

(b) IASI with constant lifetime (VD0.5)

(c) This study (NE)

(d) IASI with modelled lifetime (VDgrlf)

MFB (%)

Figure 8. Overview of the comparison with ground-based measurements of ammonia. MFB for each of the stations from AMoN, EMEP and EANET monitoring stations calculated after running LMDz-OR-INCA with the emissions of EGG, VD0.5, NE and VDgrlf for the period 2008–2017.
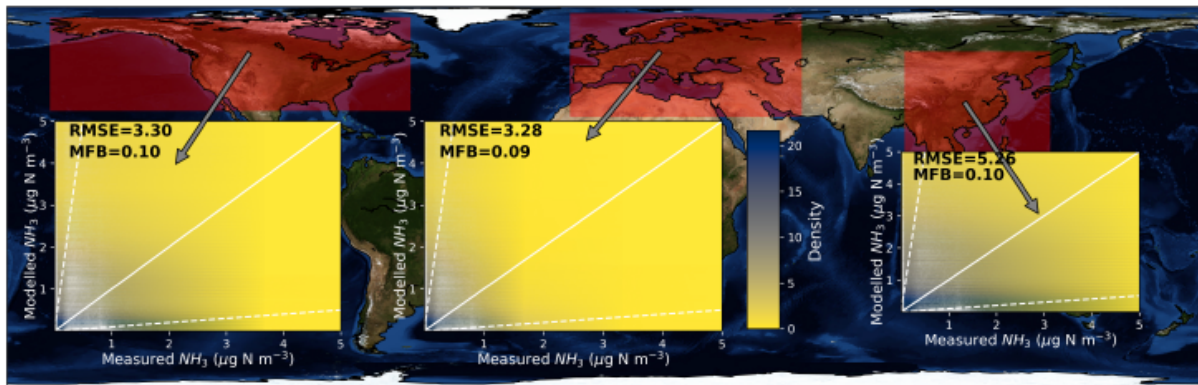
Figure 9. Kernel density estimation (KDE) of the probability density function (PDF) of modelled versus CrIS concentrations of ammonia in a non-parametric way. Modelled concentrations are results of simulations using NE emissions datasets for the period 2012–2017, for which CrIS data were available. The comparison is shown for North America, Europe and Southeastern Asia.
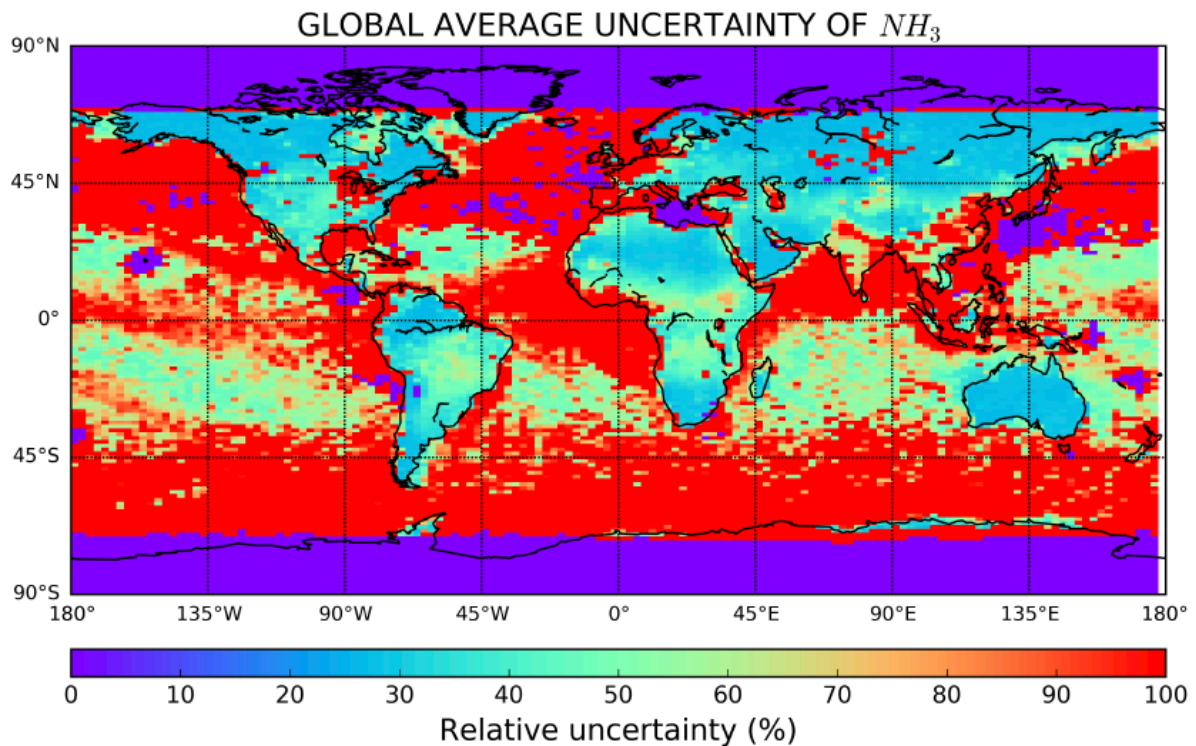
Figure 10. 10-year average relative uncertainty of modelled surface concentrations expressed as the standard deviation of surface concentrations from a model ensemble (Table 1) divided by the average.

1331   Table 1. Model ensemble simulations using different emissions for ammonia that were used in
1332   the calculations of uncertainty. Uncertainties were calculated as the standard deviation of the
1333   surface concentrations of ammonia from the 10 ensemble members for the 10-year period
1334   (2008–2017).

	Parameter perturbed	10-year average emissions (Tg yr^{-1})
Ensemble 1	$d_k = 0$ in Eq. 2	121±50.6
Ensemble 2	$d_k = 10$ in Eq. 2	175±33.3
Ensemble 3	$d_k = 20$ in Eq. 2	189±28.7
Ensemble 4	$d_k = 60$ in Eq. 2	218±15.5
Ensemble 5	$d_k = 100$ in Eq. 2	208±51.8
Ensemble 6	$d_k = 500$ in Eq. 2	223±26.5
Ensemble 7	EGG	65±2.8
Ensemble 8	VD0.5	189
Ensemble 9	NE	213±18.1
Ensemble 10	VDgrlf	201±10.4

1335

1336

1337   **SUPPLEMENTARY FIGURE LEGENDS**

1338

1339   Fig. S 1.

1340

1341   Fig. S 2.

1342

1343   Fig. S 3.

1344

1345   Fig. S 4.

1346

1347   Fig. S 5.

1348

1349   Fig. S 6.

1350

1351   Fig. S 7.

1352

1353   Fig. S 8.

1354

1355   Fig. S 9.

1356

1357   Fig. S 10.

1358

1359   Fig. S 11.